

Received 9 June 2024, accepted 3 July 2024, date of publication 8 July 2024, date of current version 16 July 2024.

Digital Object Identifier 10.1109/ACCESS.2024.3424413

RESEARCH ARTICLE

Three-Phase Diode-Clamped Four-Level PWM Inverter With Offset Voltage Injection

MIN-SUP SONG^{ID}, JAEWON KIM^{ID}, AND HWAN-HEE CHO^{ID}

Electrification System Research Department, Smart Electrical and Signaling Division, Korea Railroad Research Institute, Uiwang-si 16105, South Korea

Corresponding author: Min-Sup Song (mssong@krii.re.kr)

This work was supported by the Korea Institute of Energy Technology Evaluation and Planning (KETEP) grant funded by the Korea government (MOTIE) (20225500000110, Design and Analysis of AC/DC Hybrid Distribution Networks).

ABSTRACT In this paper, a three-phase diode-clamped four-level PWM inverter with offset voltage injection is proposed. The proposed inverter is based on multi-neighboring reference vector (discontinuous) pulse-width modulation (MNRV (D)PWM), where multiple adjacent reference vectors with different charging/discharging characteristics of the capacitors are selected depending on the location of the command voltage. These reference vectors are evenly utilized, and the duty ratio of the remaining reference vector as a degree of freedom is adjusted to satisfy the *volt-time* product. Additionally, the proposed MNRV (D)PWM can generate various (D)PWM forms by applying the offset voltage injection method. By extending the methodology applied to the four-level inverter, a general MNRV (D)PWM method applicable to general high-dimensional multilevel multiphase PWM inverters is also proposed. It is demonstrated that MNRV (D)PWM can be applied not only to dc/ac but also to dc/dc topologies. The ripple component of the dc-link voltage has been confirmed to be related to the three-phase summation of the product of the duty of the E voltage level vector and the phase current. Through various simulations and prototype experiments, the steady-state operating characteristics have been confirmed, demonstrating reduced average switching frequency and superior THD performance compared to conventional methods. Furthermore, proficient management of fluctuations in the dc-link voltage reference and sustained voltage equilibrium are exemplified.

INDEX TERMS Three-phase PWM inverter, diode-clamped, four-level, dc-link voltage balancing, offset voltage injection, multi-neighboring reference vector discontinuous PWM.

I. INTRODUCTION

Multilevel converters, including diode-clamped, flying capacitor, cascaded H-bridge topologies, and modular multilevel converters (MMC), are widely used in medium to high-power applications like renewable energy systems, motor drives, and high voltage direct current (HVDC) transmission systems. These converters provide benefits such as improved voltage/current quality, reduced switching losses, enhanced power handling, modularity, scalability, and high reliability [1], [2], [3], [4], [5], [6], [7].

The diode-clamped method is especially popular due to its simple power stage configuration. However, maintaining

balanced voltages across dc-link capacitors, particularly in higher levels like four-level or above, is challenging but essential for stable operation and enhanced performance [8], [9], [10], [11], [12]. Extensive research has focused on addressing this voltage balancing issue over the past few decades.

Common methods for voltage balancing in diode-clamped circuits include active voltage balancing circuits [13], [14], [15], model predictive control (MPC) [16], [17], [18], and artificial intelligence (AI)-based control [19], [20], [21]. Active voltage balancing circuits use additional power electronics components like choppers or active switches to transfer energy between dc-link capacitors, ensuring stable operation by real-time monitoring and precise adjustments. However, this method involves complex implementation,

The associate editor coordinating the review of this manuscript and approving it for publication was Jorge Esteban Rodas Benítez^{ID}.

additional power consumption, and limited effectiveness during rapid load changes. MPC predicts future system behavior and optimizes control inputs to achieve voltage balance, offering high performance, flexibility, and fast transient responses. Despite its advantages, MPC faces challenges like computational complexity, implementation difficulties, and model accuracy issues. AI-based methods utilize techniques such as neural networks, fuzzy logic, and genetic algorithms to optimize voltage levels by leveraging system data. Trained on historical data and simulations, these models enhance performance, efficiency, and reliability. However, AI methods present challenges including training complexity, interpretability, and hardware implementation difficulties.

Meanwhile, two widely recognized methods in the industry to address voltage balancing issues are virtual-vector PWM (VVPWM) [22], [23], [24], [25], [26] and carrier-overlapped PWM (COPWM) [27], [28], [29], [30]. VVPWM uses virtual reference vectors to ensure that the sum of related currents is zero, effectively eliminating voltage imbalances within the carrier cycle. It is easy to implement with carrier-based equivalent PWM methods [26]. However, VVPWM has high total harmonic distortion (THD) at high amplitude modulation indexes (m) and incurs relatively high switching losses due to the narrow clamping region of the outermost vectors within a 120° interval. COPWM achieves voltage balancing using intricately designed overlapping carriers with a single command voltage. This method ensures uniform duty ratios of intermediate voltage levels, naturally satisfying the *volt-time* product. However, COPWM suffers from low power quality at low m due to frequent transitions between clamp and normal modes, leading to potential noise. Additionally, it involves complex processes like calculating zero-sequence voltage for dc-link control. Both VVPWM and COPWM ideally calculate the duty ratios of reference voltage vectors, sometimes failing to satisfy the *volt-time* product during transient periods.

On the other hand, another new modulation technique, the multi-neighboring reference vector discontinuous PWM (MNRV DPWM), was introduced to address the dc-link voltage imbalance in a four-level diode-clamped ac/dc converter [31]. This method selects multiple adjacent reference vectors based on the command voltage's location, with different capacitor charging characteristics. This method achieves voltage balancing naturally by evenly utilizing the duty ratios of these vectors and integrating duty compensators to reflect the capacitors' charging characteristics. A remaining degree of freedom outmost reference vector is selected to satisfy the *volt-time* product.

MNRV DPWM has been extended to various dc/dc converters, including the full-bridge (FB) diode-clamped four-level *LLC* resonant converter [32], FB symmetric switching converter [33], FB three-level *LLC* resonant converter [34], and a half-bridge (HB) four-level *LLC* resonant converter [35]. Specifically, in the four-level symmetric switching converter, this method successfully implements a

TABLE 1. Comparison of pros and cons of the proposed method and existing methods.

	VVPWM [22]–[26]	COPWM [27]–[30]	Proposed Method
Pros	<ul style="list-style-type: none"> ·Easy implementation ·Ensures minimal dc-link voltage deviation 	<ul style="list-style-type: none"> ·Natural voltage balance ·Fast dc-link voltage dynamics 	<ul style="list-style-type: none"> ·Generality (Various DPWM types can be implemented based on the applied offset voltage, making it applicable to both inverters and dc/dc converters, and easily extendable to high-dimensional multilevel multiphase systems.) ·Superior reference voltage tracking performance ·Satisfactory THD in wide range of m
Cons	<ul style="list-style-type: none"> ·High average switching frequency (Large switching loss) ·Low THD in high m 	<ul style="list-style-type: none"> ·Somewhat complex control (calculation of zero sequence voltage) ·Low THD in low m 	<ul style="list-style-type: none"> ·Requires somewhat large capacitance ·High dc-link voltage deviation

modulation technique that injects an offset voltage using the extreme values of the reference voltage into the FB topology composed of two symmetric HBs. This indicates the potential scalability of MNRV DPWM to future multiphase multilevel converter topologies.

This paper introduces a three-phase diode-clamped four-level PWM inverter utilizing an offset voltage injection-based MNRV (D)PWM method. Originally developed for single-phase FB systems, it's now adapted to three-phase systems. This approach employs the offset voltage injection method, commonly used in traditional two-level inverters, to generate various continuous/discontinuous switching modulation schemes [36], [37], [38].

The proposed MNRV (D)PWM-based multilevel PWM inverter offers several advantages over conventional methods.

- Unlike conventional methods that design the duty ratios of reference step voltage vectors based on the command voltage and correct them later to reflect voltage deviations, the proposed method incorporates duty compensation parameters into the duty cycle calculation of the reference step voltage in real-time. This approach addresses the voltage deviations in dc-link capacitors and maintains the *volt-time* product without errors, even during transient conditions.
- The versatility of this approach allows for the generation of various DPWM types using miscellaneous offset voltages based on the extremes of the command voltage. Additionally, the application of intuitive modulation techniques makes it easy to extend to high-dimensional multilevel multiphase systems. It can also be applied in a similar way to both inverter and dc/dc converter topologies.
- The presence of a wide discontinuous switching region can lower the average switching frequency, thereby reducing switching losses.

- Additionally, it has been demonstrated to provide excellent THD performance in output current and line voltage across a wide range of modulation indices.

However, a higher capacitance value is needed for stable operation, as the proposed method permits a certain level of voltage deviation compared to conventional approaches. Table 1 compares the advantages and disadvantages of conventional methods and the proposed method.

Section II outlines the design principles for offset voltage injection-based MNRV DPWM, tailored for three-phase diode-clamped four-level PWM inverters, and extends the methodology to high-dimensional multilevel multiphase systems. It also confirms the universality of the proposed modulation method by demonstrating its applicability to both dc/ac and dc/dc topologies. In Section III, a thorough analysis of the dc-link voltage ripple component is conducted using Fast Fourier Transform (FFT) analysis of the product of the duty of the E vector and the phase current. Section IV presents simulation results, including verification of steady-state operating characteristics, comparison of THD, analysis of average switching frequency, and validation of dynamic response to dc-link voltage fluctuations. Finally, Section V confirms steady-state operation and transient behavior through prototype circuit experiments, along with verification of dc-link voltage balancing control.

II. MNRV (D)PWM FOR THREE-PHASE FOUR-LEVEL PWM INVERTER WITH OFFSET VOLTAGE INJECTION

The circuit of the proposed three-phase diode-clamped four-level PWM inverter is illustrated in Fig. 1. The dc-link stage, composed of three capacitors connected in series (C_{dc1} , C_{dc2} , and C_{dc3}), interfaces with the voltage source V_{dc} . Meanwhile, the three-phase switching stage consists of three switch groups, labeled Q_{x1} to Q_{x6} (where $x = a, b, c$), along with clamping diodes that connect each step voltage of the dc-link stage to the switching nodes. The output of each phase is then connected to either a delta- or wye-connected load. Here, the output voltage of each phase is denoted as V_{xn} , while the output current of each phase is represented as i_x .

A. OPERATION PRINCIPLES OF MNRV (D)PWM FOR THREE-PHASE DIODE-CLAMPED FOUR-LEVEL PWM INVERTER

In a three-phase system, the command voltages v_{cmd_x} have a phase difference of 120° from each other, as shown in (1) ($x = a, b, c$). The phase angle θ can be expressed as 2π times the product of the base frequency f_s of the power system and the time t . V_{CMD_x} used in MNRV (D)PWM has the value of v_{cmd_x} plus the injected offset voltage V_{offset} and normalization voltage of $0.5V_{dc}$, as shown in (2). V_{offset} takes

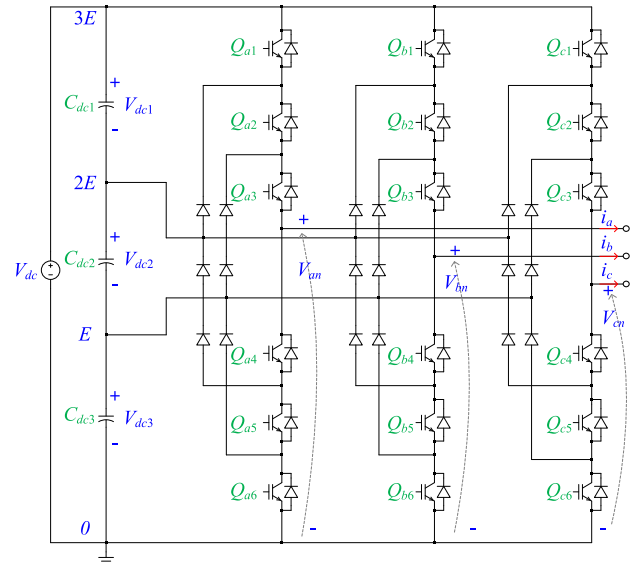


FIGURE 1. Three-phase diode-clamped four-level PWM inverter.

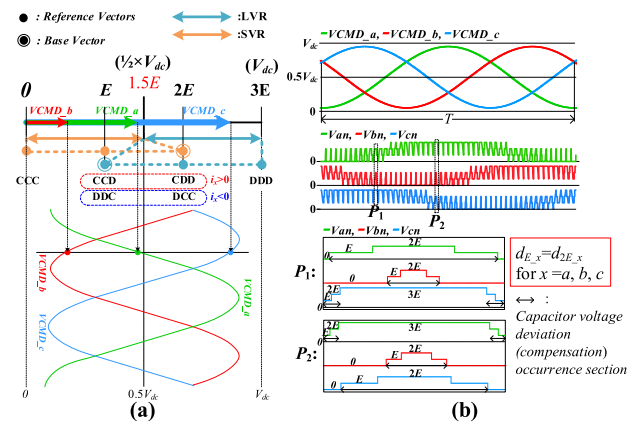


FIGURE 2. Operation principles of MNRV (D)PWM for a four-level PWM inverter applying SPWM (Voffset = 0): (a) selection of MNRVs according to the V_{CMD_x} position and (b) switching patterns with equal durations of intermediate-levels ($dE_x = d2E_x$).

various forms depending on the modulation methods.

$$\begin{cases} v_{cmd_a} = m \frac{V_{dc}}{2} \sin \theta, \\ v_{cmd_b} = m \frac{V_{dc}}{2} \sin(\theta - \frac{2\pi}{3}), \\ v_{cmd_c} = m \frac{V_{dc}}{2} \sin(\theta + \frac{2\pi}{3}). \end{cases} \quad (1)$$

$$V_{CMD_x} = v_{cmd_x} + V_{offset} + 0.5V_{dc} \quad (2)$$

Fig. 2 illustrates the implementation example of MNRV (D)PWM for a three-phase diode-clamped four-level PWM inverter applying sinusoidal PWM (SPWM). In MNRV (D)PWM, symmetry is maintained with respect to the virtual center vector, which corresponds to the $1.5E$ vector here [35]. Depending on the magnitude of V_{CMD_x} , it is primarily divided into two regions: a large vector region (LVR) when $V_{CMD_x} \geq 0.5V_{dc}$ and a small vector region (SVR) when

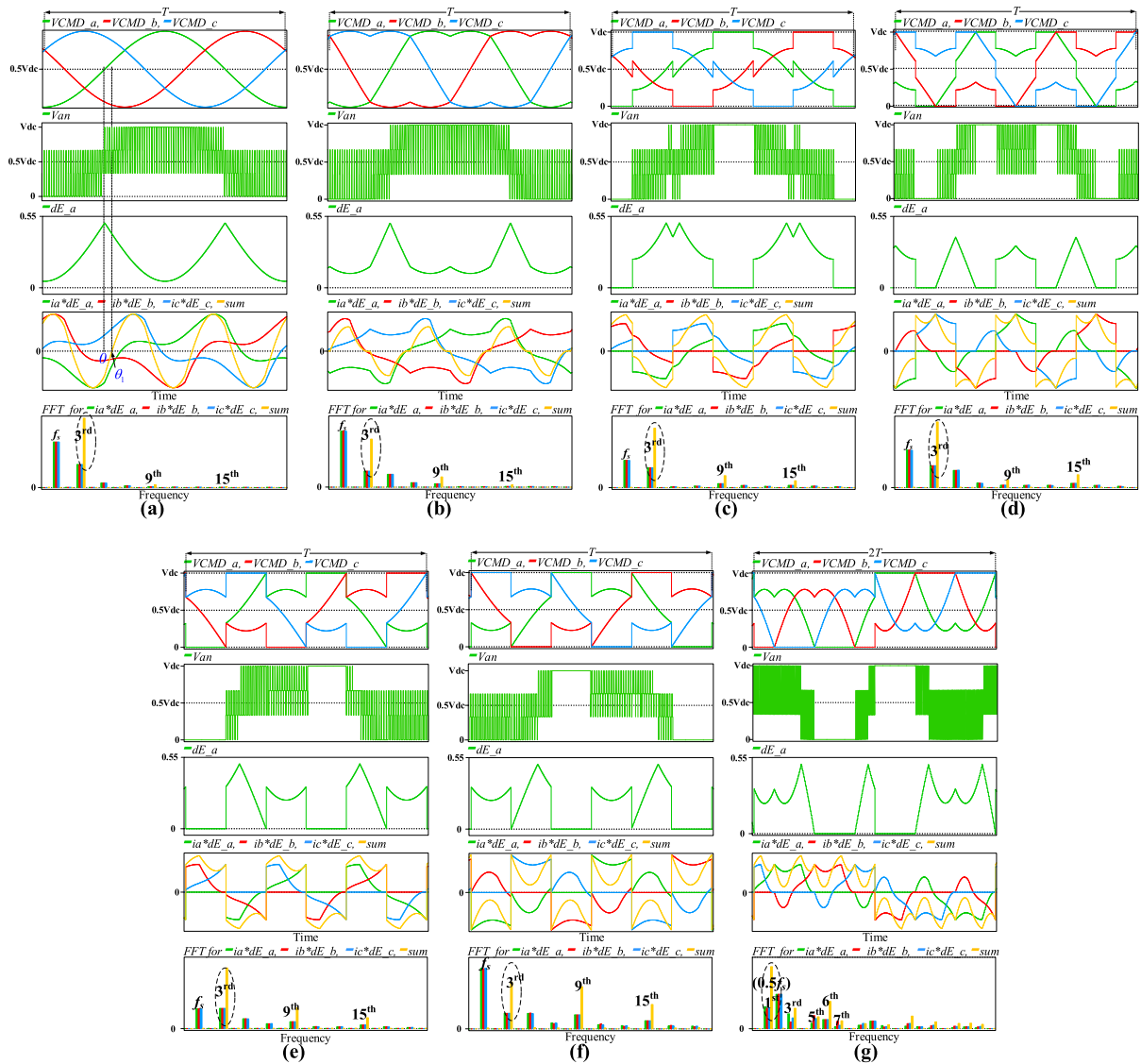


FIGURE 3. Various MNRV (D)PWM forms according to injected offset voltage types: (a) SPWM, (b) SVPWM, (c) 60°DPWM, (d) 30°DPWM, (e) 60°(+30°)DPWM, (f) 60°(-30°)DPWM, and (g) DPWMMAXorMIN.

$V_{CMD_x} < 0.5V_{dc}$. In other words, v_{cmd_x} is positive in LVR and negative in SVR. To ensure uniform control of the dc-link capacitor voltages, it is crucial to evenly utilize all reference voltage vectors capable of influencing the state of charge of the capacitors. This entails utilizing voltage vectors corresponding to all intermediate levels except for the outermost voltage levels, namely 0 and $3E$. Furthermore, to uphold the *volt-time* product, another voltage vector with a degree of freedom must be included. Therefore, to incorporate all reference vectors with distinct capacitor charging/discharging characteristics and one voltage vector for adjusting the *volt-time* product, MNRVs become E , $2E$, and $3E$ when V_{CMD_x} is in LVR, and 0 , E , and $2E$ when V_{CMD_x} belongs to SVR. Here, 0 , E , $2E$, and $3E$ refer V_0 , V_E , V_{2E} , and V_{3E} , which are 0 , $V_{dc}/3$, $V_{dc} \times 2/3$, and V_{dc} , respectively. C or D expressed under each step voltage indicates the charging/discharging state of the capacitors in the dc-link stage.

For example, the capacitor charging state at $2E$ is CDD for positive current ($i_x > 0$), which implies that C_{dc1} is charged with $2/3 \times i_x$ and C_{dc2} , C_{dc3} are discharged with $1/3 \times i_x$.

Since the a , b , and c phases can be operated independently, this method offers the advantage of linear implementation on a straight line, unlike conventional space-vector PWM (SVPWM), which considers both the magnitude and phase of the command voltage and is implemented on a two-dimensional plane. The key to maintaining capacitor voltage balance, regardless of the position of the V_{CMD_x} , is to set the duty ratios of the intermediate-level voltage vectors to be equal to each other, i.e. $d_{E_x} = d_{2E_x}$. This method effectively minimizes voltage imbalances on average by evenly utilizing all factors influencing the charging and discharging of the capacitors. To define other PWM types, we first need to define maximum and minimum values as in (3), as shown at the bottom of the next page. Here, V_{max} and V_{min} refer to the

maximum and minimum values of v_{cmd_x} , respectively, and $V_{max(min)_{\pm\pi/6}}$ refer to the maximum and minimum values of v_{cmd_x} phase shifted by $(+)\pi/6$ and $(-)\pi/6$, respectively.

By utilizing the previously defined maximum and minimum values to set V_{offset} as (4), it becomes possible to define SPWM, SVPWM, 60°DPWM, 30°DPWM, 60°(+30°)DPWM, 60°(-30°)DPWM, and DPWMMAX-orMIN.

Next, the duty compensation parameters d_{comp_x} are established as in (5), as shown at the bottom of the next page, to finely adjust each reference voltage vector. The d_{comp_x} represent values that are proportional to the difference between the average voltages on the left and right sides of the subscript underscore. For instance, d_{comp12_3} represents the proportional integral control output of the difference between $(V_{dc1} + V_{dc2})/2$ on the left side and V_{dc3} on the right side of the subscript underscore. Here, V_{dc1} , V_{dc2} , V_{dc3} denote the terminal voltages of C_{dc1} , C_{dc2} , C_{dc3} , respectively. K_p and K_I represent the proportional and integral gains of PI controller.

To maintain capacitor voltage balance, the duty cycles of intermediate-level voltage vectors are initially set to be equal. Then, the d_{comp} parameters, which are proportional to small voltage deviations occurring during actual operation, are inserted. This allows for fine adjustments to the duty ratios of each reference voltage vector during closed-loop control, ensuring precise regulation even during transient intervals.

In this manner, depending on the magnitude of V_{CMD_x} , the duty ratios of each reference voltage vector and the PWM command voltages compared to the actual carrier are expressed as shown in (6) and (7). In LVR, d_{E_x} is treated as the base vector, while in SVR, d_{2E_x} serves as the base vector. The duty ratios of the remaining intermediate-level vectors are primarily set to match that of the base vector, incorporating the d_{comp} values for precise voltage balance control. Additionally, the duty ratios of the remaining outermost voltage vectors are adjusted to fulfill the *volt-time* product requirement.

The values of d_{0_x} , d_{E_x} , d_{2E_x} , and d_{3E_x} represent the duty ratios of reference vectors 0, E, 2E, and 3E for x phase, respectively. PWM_CMD_x1 , PWM_CMD_x2 , and PWM_CMD_x3 denote the PWM command voltages corresponding to the upper switches of phase x, namely Q_{x1} , Q_{x2} , and Q_{x3} , respectively. These values are compared with the carrier signal to generate the PWM output signal. N_{max} denotes period value of the carrier. To modulate the effect of the d_{comp} based on the sign of the output current i_x , the $sgn()$ function, which outputs the polarity of the input variable, is defined as shown in (8). The definition of i_x is provided in (9) along with the amplitude of I_m , and δ is related to the power factor pf according to (10).

Fig. 3 depicts the PWM command voltages, output voltage of a phase, duty ratio of the E-level voltage vector for a phase, the product of phase current and the duty ratio of the corresponding phase's E voltage vector, and their FFT results for SPWM, SVPWM, and various DPWMs.

The command voltage patterns for widely known offset voltage injection-based (D)PWM are observed across all modulation methods [36], [37], [38]. Additionally, in DPWMs, we can observe that switching actions halt during discontinuous modulation intervals. Furthermore, in LVR, the output phase voltage takes on values of E, 2E, and 3E, while in SVR, it takes on values of 0, E, and 2E. The three-phase sum of the product of phase current and duty ratios of the intermediate voltage level (E or 2E) vectors is closely related to the capacitor voltage deviation, which will be elaborated on in Section III.

$$\begin{aligned}
 & \underline{\text{For } V_{CMD_x} \geq 0.5V_{dc}(@LVR)} \\
 & \text{if } (V_{CMD_x} == V_{dc}) \\
 & \{ \\
 & \quad \begin{pmatrix} d_{0_x} \\ d_{E_x} \\ d_{2E_x} \\ d_{3E_x} \end{pmatrix} = \begin{pmatrix} 0 \\ 0 \\ 0 \\ 1 \end{pmatrix}, \\
 & \quad \begin{pmatrix} PWM_CMD_x1 \\ PWM_CMD_x2 \\ PWM_CMD_x3 \end{pmatrix} = N_{max} \begin{pmatrix} 1 \\ 1 \\ 1 \end{pmatrix}, \\
 & \} \\
 & \text{else} \\
 & \{ \\
 & \quad \begin{pmatrix} d_{0_x} \\ d_{E_x} \\ d_{2E_x} \\ d_{3E_x} \end{pmatrix} = \begin{pmatrix} 0 \\ -\frac{V_{CMD_x}}{V_{dc}} + \frac{1}{3}sgn(i_x)d_{comp1_23} + 1 \\ -\frac{V_{CMD_x}}{V_{dc}} - \frac{2}{3}sgn(i_x)d_{comp1_23} + 1 \\ -1 + 2\frac{V_{CMD_x}}{V_{dc}} + \frac{1}{3}sgn(i_x)d_{comp1_23} \end{pmatrix}, \\
 & \quad \begin{pmatrix} PWM_CMD_x1 \\ PWM_CMD_x2 \\ PWM_CMD_x3 \end{pmatrix} = N_{max} \begin{pmatrix} d_{3E_x} \\ d_{2E_x} + d_{3E_x} \\ 1 \end{pmatrix}. \\
 & \} \tag{6}
 \end{aligned}$$

B. EXTENTION TO MULTI-PHASE AND HIGH-LEVEL TOPOLOGIES

The proposed modulation method can be easily extended to multi-phase, high-dimensional multilevel topologies. Fig. 4 illustrates the implementation example of MNRV (D)PWM for a typical high-dimensional N-level power system with p phases. Depending on whether V_{CMD_x} falls above or below the virtual center point $(N - 1)/2 \cdot E$ vector, it belongs to LVR or SVR. In LVR, MNRVs cover the switching range of E, 2E, ..., (N - 1)·E vectors, while in SVR, MNRVs operate within 0, E, ..., (N - 2)·E vectors. The duty cycles of all intermediate voltage levels, excluding the outermost voltage levels of 0 and (N - 1)·E vectors, are initially set to be equal, and fine adjustments are made by d_{comp} parameters. The switches' duty ratios and PWM command values are expressed as shown in (11), as shown at the bottom of page 8, and (12), as shown at the bottom of page 9. The duty com-

pensation parameter $d_{comp12\dots k_{(k+1)(k+2)\dots(N-1)}}$ in a general N -level case is given by (13), as shown at the bottom of page 9, for $1 \leq k \leq N - 2$. This parameter is proportional to the voltage difference between the average voltages on the left and right sides of the subscript underscore.

For $V_{CMD_x} < 0.5V_{dc}(@SVR)$

if $(V_{CMD_x} == 0)$

{

$$\begin{pmatrix} d_{0_x} \\ d_{E_x} \\ d_{2E_x} \\ d_{3E_x} \end{pmatrix} = \begin{pmatrix} 1 \\ 0 \\ 0 \\ 0 \end{pmatrix},$$

$$\begin{pmatrix} PWM_CMD_x1 \\ PWM_CMD_x2 \\ PWM_CMD_x3 \end{pmatrix} = \begin{pmatrix} 0 \\ 0 \\ 0 \end{pmatrix},$$

}

else

{

$$\begin{pmatrix} d_{0_x} \\ d_{E_x} \\ d_{2E_x} \\ d_{3E_x} \end{pmatrix} = \begin{pmatrix} 1 - 2 \frac{V_{CMD_x}}{V_{dc}} + \frac{1}{3} \text{sgn}(i_x) d_{comp12_3} \\ \frac{V_{CMD_x}}{V_{dc}} - \frac{2}{3} \text{sgn}(i_x) d_{comp12_3} \\ \frac{V_{CMD_x}}{V_{dc}} + \frac{1}{3} \text{sgn}(i_x) d_{comp12_3} \\ 0 \end{pmatrix},$$

$$\begin{pmatrix} PWM_CMD_x1 \\ PWM_CMD_x2 \\ PWM_CMD_x3 \end{pmatrix} = N_{\max} \begin{pmatrix} 0 \\ d_{2E_x} \\ d_{E_x} + d_{2E_x} \end{pmatrix}.$$

}

$$\text{sgn}(x) = \begin{cases} +1, & \text{for } x \geq 0 \\ -1, & \text{for } x < 0 \end{cases} \quad (8)$$

$$\begin{cases} i_a = I_m \sin(\theta - \delta), \\ i_b = I_m \sin(\theta - \frac{2\pi}{3} - \delta), \\ i_c = I_m \sin(\theta + \frac{2\pi}{3} - \delta). \end{cases} \quad (9)$$

$$\cos \delta = pf \quad (10)$$

$$\begin{cases} V_{\max} = \max(v_{cmd_a}, v_{cmd_b}, v_{cmd_c}), \\ V_{\min} = \min(v_{cmd_a}, v_{cmd_b}, v_{cmd_c}), \\ V_{\max_+\pi/6} = \max(v_{cmd_a}(\theta + \frac{\pi}{6}), v_{cmd_b}(\theta + \frac{\pi}{6}), v_{cmd_c}(\theta + \frac{\pi}{6})), \\ V_{\min_+\pi/6} = \min(v_{cmd_a}(\theta + \frac{\pi}{6}), v_{cmd_b}(\theta + \frac{\pi}{6}), v_{cmd_c}(\theta + \frac{\pi}{6})), \\ V_{\max_-\pi/6} = \max(v_{cmd_a}(\theta - \frac{\pi}{6}), v_{cmd_b}(\theta - \frac{\pi}{6}), v_{cmd_c}(\theta - \frac{\pi}{6})), \\ V_{\min_-\pi/6} = \min(v_{cmd_a}(\theta - \frac{\pi}{6}), v_{cmd_b}(\theta - \frac{\pi}{6}), v_{cmd_c}(\theta - \frac{\pi}{6})). \end{cases} \quad (3)$$

$$V_{offset} = \begin{cases} SPWM : 0 \\ SVPWM : -0.5(V_{\max} + V_{\min}) \\ 60^\circ DPWM : \begin{cases} 0.5V_{dc} - V_{\max}, & \text{for } V_{\max} + V_{\min} \geq 0 \\ -0.5V_{dc} - V_{\min}, & \text{for } V_{\max} + V_{\min} < 0 \end{cases} \\ 30^\circ DPWM : \begin{cases} -0.5V_{dc} - V_{\min}, & \text{for } V_{\max} + V_{\min} \geq 0 \\ 0.5V_{dc} - V_{\max}, & \text{for } V_{\max} + V_{\min} < 0 \end{cases} \\ 60^\circ(+30^\circ) DPWM : \begin{cases} 0.5V_{dc} - V_{\max}, & \text{for } V_{\max_-\pi/6} + V_{\min_-\pi/6} \geq 0 \\ -0.5V_{dc} - V_{\min}, & \text{for } V_{\max_-\pi/6} + V_{\min_-\pi/6} < 0 \end{cases} \\ 60^\circ(-30^\circ) DPWM : \begin{cases} 0.5V_{dc} - V_{\max}, & \text{for } V_{\max_+\pi/6} + V_{\min_+\pi/6} \geq 0 \\ -0.5V_{dc} - V_{\min}, & \text{for } V_{\max_+\pi/6} + V_{\min_+\pi/6} < 0 \end{cases} \\ DPWM MAX or MIN : \begin{cases} 0.5V_{dc} - V_{\max}, & \text{for } CM = 1 (V_{dc1} > V_{dc3}) \\ -0.5V_{dc} - V_{\min}, & \text{for } CM = -1 (V_{dc1} < V_{dc3}) \end{cases} \end{cases} \quad (4)$$

$$d_{comp12_3} = K_P \left(\frac{V_{dc1} + V_{dc2}}{2} - V_{dc3} \right) + K_I \int_0^t \left(\frac{V_{dc1} + V_{dc2}}{2} - V_{dc3} \right) dt,$$

$$d_{comp1_23} = K_P \left(V_{dc1} - \frac{V_{dc2} + V_{dc3}}{2} \right) + K_I \int_0^t \left(V_{dc1} - \frac{V_{dc2} + V_{dc3}}{2} \right) dt. \quad (5)$$

E voltage vector for each phase during the $T/6$ period are described by (16). Therefore, ΔV_{dc1} is determined as the integral of the three-phase sum of $d_{E-x} \cdot i_x$ during $\pi/3$ period, divided by the product of the capacitance C_{dc} and the angular frequency ω as presented in (17). As illustrated earlier in Fig. 3(a), the summation function of $d_{E-x} \cdot i_x$ exhibits periodicity of $3f_s$, delayed by θ_1 from the $0.5V_{dc}$ crossing point of V_{CMD_a} . Here, θ_1 indicates the point where the sum of $d_{E-x} \cdot i_x$ becomes 0 and it is obtained as outlined in (18).

$$\begin{cases} \Delta V_{dc1} = \frac{T_{smp1}}{C_{dc}} \sum_{x=a,b,c} d_{E-x} i_x, \\ \Delta V_{dc2} = 0, \\ \Delta V_{dc3} = -\frac{T_{smp1}}{C_{dc}} \sum_{x=a,b,c} d_{E-x} i_x, \\ \Delta V_{dc} = \Delta V_{dc1} - \Delta V_{dc3} = \frac{2T_{smp1}}{C_{dc}} \sum_{x=a,b,c} d_{E-x} i_x. \end{cases} \quad (15)$$

$$\begin{cases} \Delta V_{dc1_x} = \frac{T_{smp1}}{C_{dc}} (d_{2E-x} \frac{2}{3} i_x + d_{E-x} \frac{1}{3} i_x) = \frac{T_{smp1}}{C_{dc}} d_{E-x} i_x \\ \Delta V_{dc2_x} = \frac{T_{smp1}}{C_{dc}} (-d_{2E-x} \frac{1}{3} i_x + d_{E-x} \frac{1}{3} i_x) = 0 \\ \Delta V_{dc3_x} = \frac{T_{smp1}}{C_{dc}} (-d_{2E-x} \frac{1}{3} i_x - d_{E-x} \frac{2}{3} i_x) = -\frac{T_{smp1}}{C_{dc}} d_{E-x} i_x \end{cases} \quad (14)$$

$$\begin{aligned} \theta &: [0, \pi/3] \\ \begin{cases} d_{E_a} = -\frac{V_{CMD_a}}{V_{dc}} + 1 = \frac{1}{2} - \frac{1}{2} m \sin \theta \\ d_{E_b} = \frac{V_{CMD_b}}{V_{dc}} = \frac{1}{2} + \frac{1}{2} m \sin(\theta - \frac{2\pi}{3}) \\ d_{E_c} = -\frac{V_{CMD_c}}{V_{dc}} + 1 = \frac{1}{2} - \frac{1}{2} m \sin(\theta + \frac{2\pi}{3}) \end{cases} \end{aligned} \quad (16)$$

For $V_{CMD_x} \geq 0.5V_{dc}(@LVR)$

if ($V_{CMD_x} == V_{dc}$)

{

$$\begin{pmatrix} d_{0_x} \\ d_{E_x} \\ \dots \\ d_{(N-2)E_x} \\ d_{(N-1)E_x} \end{pmatrix} = \begin{pmatrix} 0 \\ 0 \\ \dots \\ 0 \\ 1 \end{pmatrix},$$

$$\begin{pmatrix} PWM_CMD_x1 \\ PWM_CMD_x2 \\ \dots \\ PWM_CMD_x(N-1) \end{pmatrix} = N_{max} \begin{pmatrix} 1 \\ 1 \\ \dots \\ 1 \end{pmatrix},$$

}

else

{

d_{E_x}

$$= \left\{ \begin{aligned} &-\frac{2V_{CMD_x}}{(N-2)V_{dc}} + (\text{sgn}(i_x) d_{comp12\dots(N-3)_ (N-2)_ (N-1)}) \cdot \frac{2(N-3)}{(N-1)(N-2)} \\ &+ (\text{sgn}(i_x) d_{comp12\dots(N-4)_ (N-3)_ (N-2)_ (N-1)}) \cdot \frac{2(N-4)}{(N-1)(N-2)} + \dots \\ &+ (\text{sgn}(i_x) d_{comp1_23\dots(N-1)}) \cdot \frac{2}{(N-1)(N-2)} + \frac{2}{N-2} \end{aligned} \right\},$$

$$\begin{pmatrix} d_{0_x} \\ d_{E_x} \\ d_{2E_x} \\ \dots \\ d_{(N-2)E_x} \\ d_{(N-1)E_x} \end{pmatrix} = \begin{pmatrix} 0 \\ d_{E_x} \\ d_{E_x} - \text{sgn}(i_x) \cdot d_{comp12\dots(N-3)_ (N-2)_ (N-1)} \\ \dots \\ d_{E_x} - \text{sgn}(i_x) \cdot d_{comp1_23\dots(N-1)} \\ 1 - d_{E_x} - d_{2E_x} - \dots - d_{(N-2)E_x} \end{pmatrix},$$

$$\begin{pmatrix} PWM_CMD_x1 \\ PWM_CMD_x2 \\ \dots \\ PWM_CMD_x(N-2) \\ PWM_CMD_x(N-1) \end{pmatrix} = N_{max} \begin{pmatrix} d_{(N-1)E_x} \\ d_{(N-2)E_x} + d_{(N-1)E_x} \\ \dots \\ d_{2E_x} + d_{3E_x} + \dots + d_{(N-1)E_x} \\ 1 \end{pmatrix}.$$

}

(11)

$$\begin{aligned} \Delta V_{dc1} &= \frac{1}{C_{dc}} \int_{\langle T/6 \rangle} \sum_{x=a,b,c} d_{E_x} i_x dt \\ &= \frac{T}{2\pi C_{dc}} \left[- \int_0^{\theta_1} \sum_{x=a,b,c} d_{E_x} i_x d\theta + \int_{\theta_1}^{\pi/3} \sum_{x=a,b,c} d_{E_x} i_x d\theta \right] \end{aligned} \tag{17}$$

$$\theta_1 = 0.5 \times \left\{ \frac{\pi}{3} + \delta - \cos^{-1} \left(\frac{\cos \delta}{2} \right) \right\} \tag{18}$$

For SPWM,

$$\Delta V_{dc1} = \frac{mI_m T}{8\pi C_{dc}} \cdot \left[\begin{array}{l} -\sin \delta + \left\{ \delta - \cos^{-1} \left(\frac{\cos \delta}{2} \right) \right\} \cdot \cos \delta \\ + \sqrt{4 - \cos^2 \delta} \end{array} \right] \tag{19}$$

For SVPWM,

$$\Delta V_{dc1} = \begin{cases} \frac{mI_m T}{16\pi C_{dc}} \cdot \left\{ \begin{array}{l} (-6 + 2\sqrt{3}\delta) \sin \delta \\ + (2\sqrt{3} - \pi + 6\delta) \cos \delta \end{array} \right\}, & \text{for } \delta \leq \frac{\pi}{6} \\ \frac{\sqrt{3} mI_m T \sin \delta}{48C_{dc}}, & \text{for } \delta > \frac{\pi}{6} \end{cases} \tag{20}$$

For $V_{CMD_x} < 0.5V_{dc}(@SVR)$

if ($V_{CMD_x} == 0$)

$$\left\{ \begin{array}{l} \begin{pmatrix} d_{0_x} \\ d_{E_x} \\ \dots \\ d_{(N-2)E_x} \\ d_{(N-1)E_x} \end{pmatrix} = \begin{pmatrix} 1 \\ 0 \\ \dots \\ 0 \\ 0 \end{pmatrix}, \\ \begin{pmatrix} PWM_CMD_x1 \\ PWM_CMD_x2 \\ \dots \\ PWM_CMD_x(N-1) \end{pmatrix} = \begin{pmatrix} 0 \\ 0 \\ \dots \\ 0 \end{pmatrix}, \end{array} \right.$$

else

$$\left\{ \begin{array}{l} d_{(N-2)E_x} = \left\{ \begin{array}{l} \frac{2V_{CMD_x}}{(N-2)V_{dc}} + (\text{sgn}(i_x) d_{comp12\dots(N-2)_ (N-1)}) \cdot \frac{2}{(N-1)(N-2)} \\ + (\text{sgn}(i_x) d_{comp12\dots(N-3)_ (N-2)_ (N-1)}) \cdot \frac{1}{(N-1)(N-2)} + \dots \\ + (\text{sgn}(i_x) d_{comp12_34\dots(N-1)}) \cdot \frac{1}{(N-1)(N-2)} \end{array} \right\}, \\ \begin{pmatrix} d_{0_x} \\ d_{E_x} \\ \dots \\ d_{(N-3)E_x} \\ d_{(N-2)E_x} \\ d_{(N-1)E_x} \end{pmatrix} = \begin{pmatrix} 1 - d_{E_x} - d_{2E_x} - \dots - d_{(N-2)E_x} \\ d_{(N-2)E_x} - \text{sgn}(i_x) \cdot d_{comp12\dots(N-2)_ (N-1)} \\ \dots \\ d_{(N-2)E_x} - \text{sgn}(i_x) \cdot d_{comp12_34\dots(N-1)} \\ d_{(N-2)E_x} \\ 0 \end{pmatrix}, \\ \begin{pmatrix} PWM_CMD_x1 \\ PWM_CMD_x2 \\ \dots \\ PWM_CMD_x(N-2) \\ PWM_CMD_x(N-1) \end{pmatrix} = N_{max} \begin{pmatrix} 0 \\ d_{(N-2)E_x} \\ \dots \\ d_{2E_x} + \dots + d_{(N-2)E_x} \\ d_{E_x} + d_{2E_x} + \dots + d_{(N-2)E_x} \end{pmatrix}. \end{array} \right.$$

(12)

$d_{comp12\dots k_ (k+1)_ (k+2)\dots(N-1)}$

$$= K_P \left(\frac{\sum_{n=1}^k V_{dcn}}{k} - \frac{\sum_{n=k+1}^{N-1} V_{dcn}}{N-k-1} \right) + K_I \int_0^t \left(\frac{\sum_{n=1}^k V_{dcn}}{k} - \frac{\sum_{n=k+1}^{N-1} V_{dcn}}{N-k-1} \right) dt. \tag{13}$$

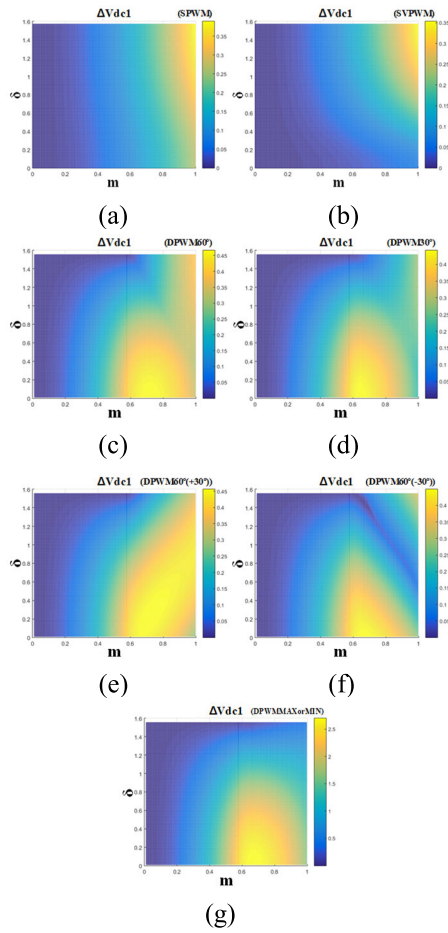


FIGURE 6. Numerical analysis results of ΔV_{dc1} according to m and δ for (a) SPWM, (b) SVPWM, (c) 60°DPWM, (d) 30°DPWM, (e) 60°(+30°)DPWM, (f) 60°(-30°)DPWM, and (g) DPWMMAXorMIN.

For $m < 0.57735$

$$\Delta V_{dc1} = \begin{cases} \frac{3mI_m T \cos \delta}{4C_{dc}}, & \text{for DPWMMAXorMIN} \\ \frac{mI_m T \cos \delta}{8C_{dc}}, & \text{for other DPWMs.} \end{cases} \quad (21)$$

Consequently, the determination of ΔV_{dc1} for SPWM is elucidated by (19). Applying a similar approach, ΔV_{dc1} for SVPWM can be derived as shown in (20). In SVPWM, it can be observed that ΔV_{dc1} is divided into two parts depending on the magnitude of the phase delay δ between the output phase current and the reference command voltage.

DPWMMAXorMIN and other forms of DPWM satisfy (21) when $m < 0.57735$. However, due to the variability in scenarios based on the values of m and δ , analytical investigation is required for the remaining DPWM methods rather than explicit equations. Fig. 6 illustrates ΔV_{dc1} for SPWM, SVPWM, and various DPWM methods under the conditions of $V_{dc} = 200V$, load impedance of 22.71Ω , $C_{dc} = 7.5mF$, and $f_s = 60Hz$. Here, the horizontal and vertical axes represent m and δ . ΔV_{dc1} is depicted using contour lines, reflecting

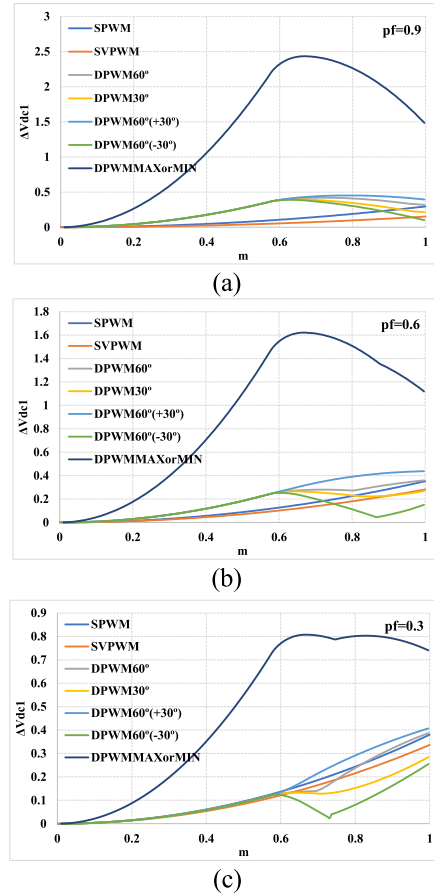


FIGURE 7. ΔV_{dc1} comparisons of various MNRV (D)PWMs for (a) $pf = 0.9$, (b) $pf = 0.6$, and (c) $pf = 0.3$.

changes in values across the axes. The darker shades of blue represent lower values of ΔV_{dc1} , while the darker shades of yellow indicate higher values.

Fig. 7 directly compares the ΔV_{dc1} values for various modulations. Generally, an increase in m leads to an increase in ΔV_{dc1} , while a decrease in the pf results in a decrease in ΔV_{dc1} . For all DPWM methods, when $m < 0.57735$, ΔV_{dc1} is expressed as given in (21). However, beyond this threshold, there exists a region where ΔV_{dc1} decreases as m increases. Therefore, at lower pf and higher values of m , DPWM methods such as 30°DPWM or 60°(-30°)DPWM exhibit smaller ΔV_{dc1} regions compared to SPWM or SVPWM. DPWMMAXorMIN, which utilizes CM, tends to maintain continuous charging or discharging of V_{dc1} over one fundamental cycle, resulting in higher ΔV_{dc1} values compared to other methods. However, as the pf decreases, the difference between DPWMMAXorMIN and other methods gradually diminishes.

IV. SIMULATIONS

A. OPERATING WAVEFORM

The main operation waveforms of the proposed offset voltage injection-based MNRV (D)PWM are illustrated in Fig. 8

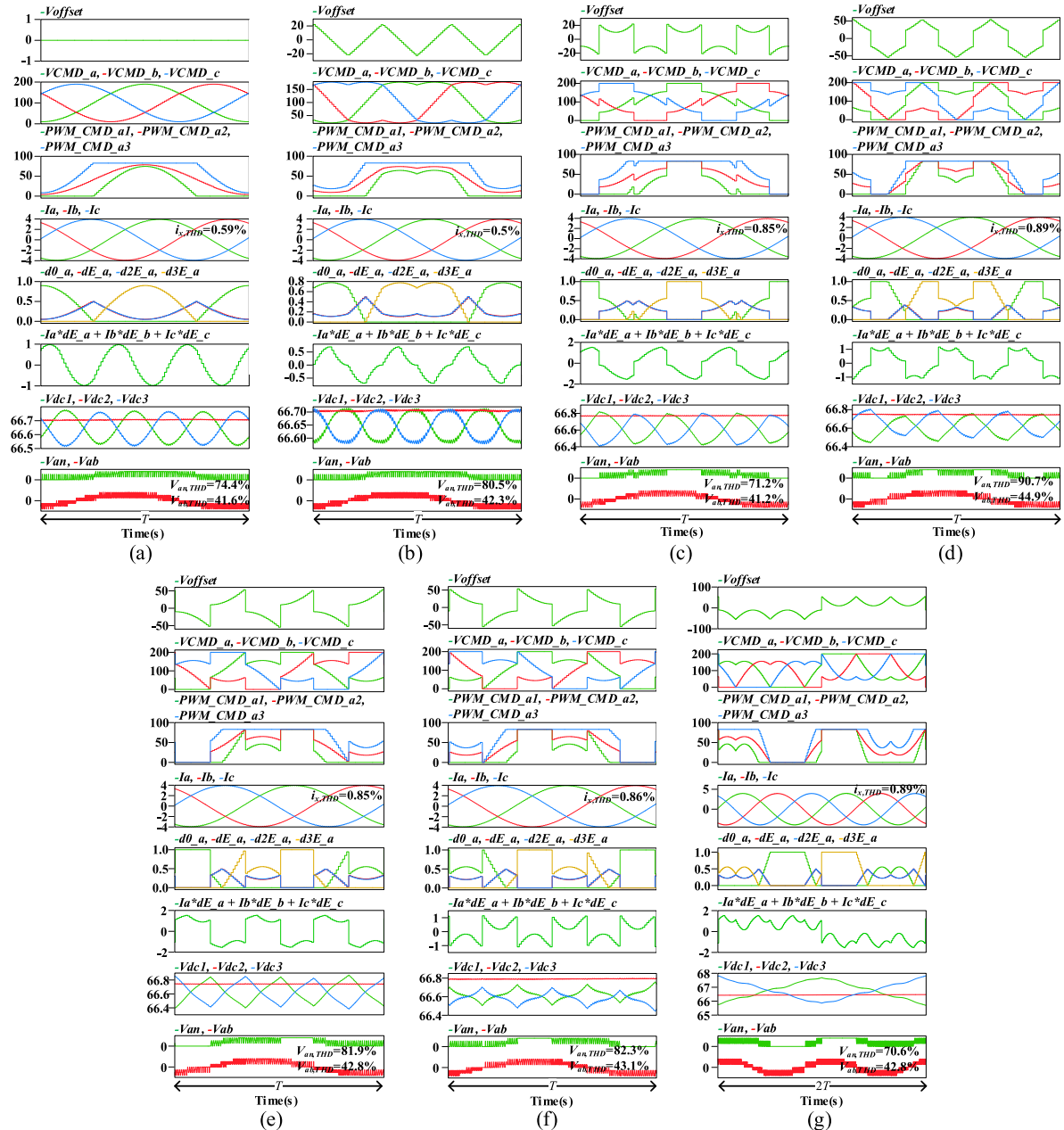


FIGURE 8. Steady-State operating waveforms for the proposed offset voltage injection-based MNRV(D)PWM for (a) SPWM, (b) SVPWM, (c) 60°DPWM, (d) 30°DPWM, (e) 60°(+30°)DPWM, (f) 60°(-30°)DPWM, and (g) DPWMMAXorMIN.

along with simulation results. Under the simulation conditions of $V_{dc} = 200\text{V}$, load impedance of 22.71Ω , $m = 0.9$, $m_f = 100$, $pf = 0.9$, $C_{dc} = 7.5\text{mF}$, and $f_s = 60\text{Hz}$, unique characteristics of seven different MNRV (D)PWM methods were observed based on various offset voltage injection methods as described in (4).

Unlike VVPWM, the clamp interval of the outermost vectors is observed to be 180° , indicating lower switching losses. THD in the output current was lowest in SVPWM at 0.5%, slightly higher in SPWM at 0.59%, and approximately 0.85~0.89% in the remaining DPWMs.

The THD in the output phase voltage was lowest in DPWMMAXorMIN at 70.6% and highest in 30°DPWM at 90.7%. The THD in the line voltage ranged from 41.2% to 44.9%. As observed earlier, the three-phase sum of $dE_x \cdot i_x$ appears to be closely related to the charging and discharging profiles of V_{dc1} or V_{dc3} . In fifth rows, the values of dE_{-a} and $d2E_{-a}$ are nearly identical, indicating a very small value of d_{comp} .

Under the same conditions, simulations for VVPWM and COPWM were conducted for comparison (see Fig. 9). Unlike MNRV (D)PWM methods where the clamp interval of the outermost vectors is 180° , VVPWM exhibits a 120° interval.

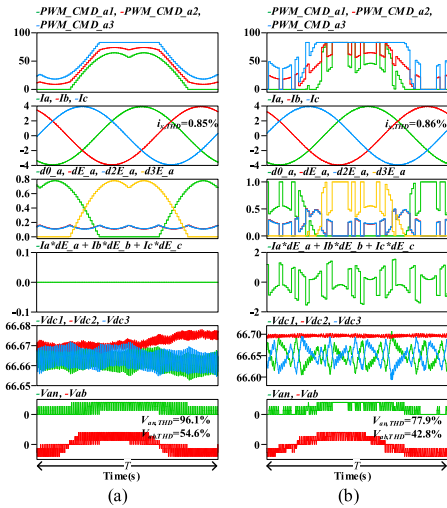
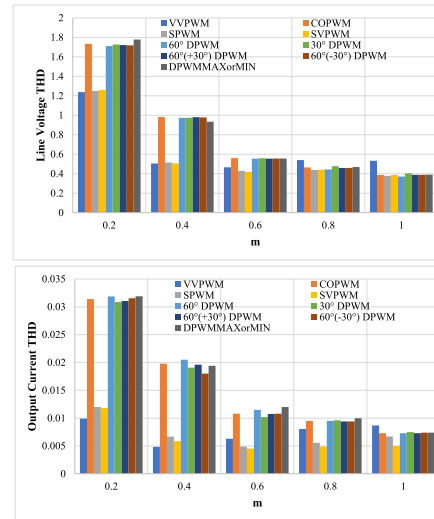


FIGURE 9. Steady-state operating waveforms for the existing (a) VVPWM and (b) COPWM.

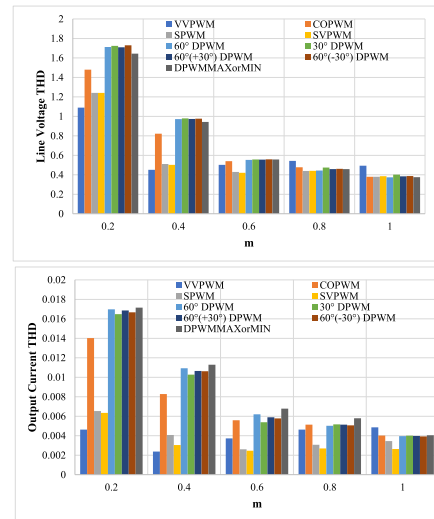
As a result, while VVPWM endures more switching losses, significantly reduced dc-link voltage ripple is observed under steady-state conditions due to the broader active switching intervals. Additionally, COPWM, by segmenting the switching regions around $0.5V_{dc}$ and maintaining consistent duty ratios for intermediate voltage levels, demonstrates operation characteristics almost similar to the proposed MNRV (D)PWM. However, COPWM differs from the proposed method in injecting a new type of zero-sequence voltage per control cycle to form a current closest to the required neutral-point current. However, in COPWM, frequent transitions between clamp and non-clamp regions are observed due to the update of the zero-sequence voltage to its optimal value for dc-link voltage balance in every control cycle. While this approach minimizes capacitor voltage imbalances, the high-frequency distortion components included in the PWM command may adversely affect current or voltage components. The THD in the output current for both VVPWM and COPWM was approximately 0.85%. However, due to the higher switching frequency in VVPWM, relatively higher THD values were observed in the output voltage and line voltage.

B. THD ANALYSIS

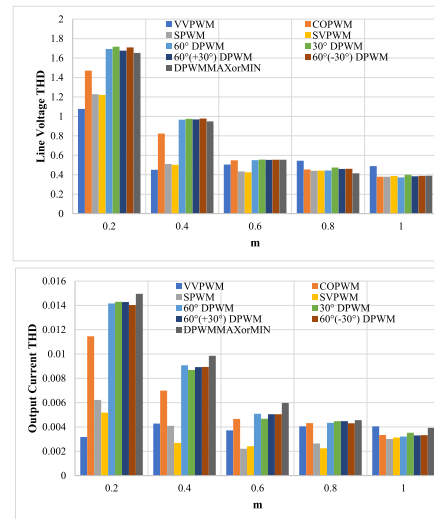
A comprehensive analysis of THD on the output line voltage and output phase current for VVPWM, COPWM, and proposed MNRV (D)PWM schemes is presented in Fig. 10. The THD comparison results for $pf = 0.9$, $pf = 0.6$, and $pf = 0.3$ are illustrated in Figs. 10(a), (b), and (c), respectively. It is observed that VVPWM exhibits outstanding THD performance for both line voltage and output current at low m . However, as m increases, the THD performance of MNRV(D)PWM methods gradually improves. Especially for the line voltage, satisfactory THD performance of the proposed MNRV (D)PWM is observed at $m > 0.8$, while



(a)



(b)



(c)

FIGURE 10. Comparative analysis of total harmonic distortions for line voltage and output current at (a) $pf = 0.9$, (b) $pf = 0.6$, and (c) $pf = 0.3$.

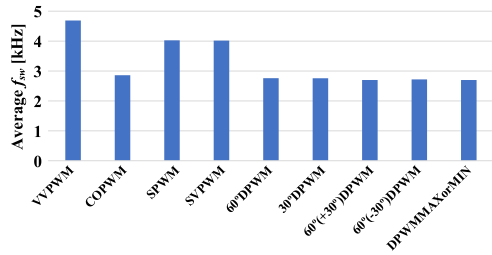


FIGURE 11. Comparison for average switching frequency.

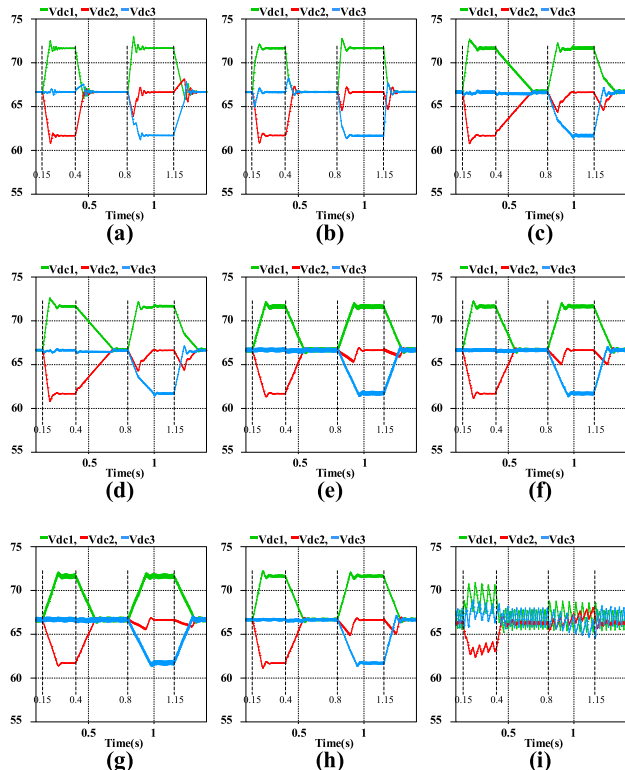


FIGURE 12. Comparison of dynamic characteristics for step changes in dc-link voltage for (a) VVPWM, (b) COPWM, (c) SPWM, (d) SVPWM, (e) 60°DPWM, (f) 30°DPWM, (g) 60°(+30°)DPWM, (h) 60°(-30°)DPWM, and (i) DPWMMAXorMIN.

for the output current, SPWM and SVPWM exhibit superior characteristics compared to VVPWM at $m > 0.6$. Moreover, as m approaches 1, all MNRV (D)PWM methods demonstrate commendable THD performance. Furthermore, COPWM shows lower THD performance compared to continuous MNRV PWM methods (SPWM, SVPWM), while demonstrating similar performance to MNRV DPWMs.

C. AVERAGE SWITCHING FREQUENCY

Under the conditions of $f_s = 60\text{Hz}$, $m_f = 100$, and $m = 0.9$, the average switching frequencies for VVPWM, COPWM, and the proposed MNRV (D)PWM were compared in Fig. 11. For VVPWM, PWM_CMD_a1 and PWM_CMD_a3 each have a switching pause period of 120° . As a result, the individual switching frequencies for Q_{a1} and Q_{a3} are calculated to be 4kHz ($6\text{kHz} \times 2/3$), resulting in an average switching

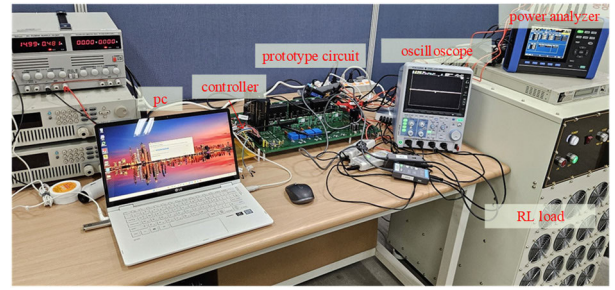


FIGURE 13. Experimental setup for prototype circuit.

frequency of 4.6kHz ($((4k + 6k + 4k)/3)$). On the other hand, for MNRV-based SPWM and SVPWM, PWM_CMD_a1 and PWM_CMD_a3 have a switching pause period of 180° . Therefore, the individual switching frequencies of Q_{a1} and Q_{a3} are calculated to be 3kHz ($6\text{kHz} \times 1/2$), resulting in an average switching frequency of 4kHz ($((3k + 6k + 3k)/3)$). For MNRV DPWMs, there is an additional 60° clamp period in addition to the 180° switching rest period. As a result, the average switching frequency is calculated to be 2.6kHz ($((2k + 4k + 2k)/3)$). COPWM shares similarities with MNRV DPWM in that it has a clamp period, but its actual switching frequency is slightly higher due to frequent movement between clamp intervals and continuous intervals. Therefore, the actual average switching frequency is slightly higher than 2.6 kHz. In conclusion, for MNRV DPWM, as m approaches 1, the average switching frequency decreases while the THD performance of the phase current is superior to that of VVPWM.

D. DYNAMICS OF DC-LINK VOLTAGE STEP CHANGES

The comparison of dynamic characteristics in response to sudden voltage fluctuations of the dc-link voltage reference is illustrated in Fig. 12.

Initially, the dc-link voltages are set as $V_{dc1} = V_{dc2} = V_{dc3} = 66.6\text{V}$. At $t = 0.15\text{s}$, these voltages are stepped to $V_{dc1} = 71.6\text{V}$, $V_{dc2} = 61.6\text{V}$, $V_{dc3} = 66.6\text{V}$. After a certain stabilization period, at $t = 0.4\text{s}$, they revert to $V_{dc1} = V_{dc2} = V_{dc3} = 66.6\text{V}$. At $t = 0.8\text{s}$, the voltages are stepped to $V_{dc1} = 71.6\text{V}$, $V_{dc2} = 66.6\text{V}$, $V_{dc3} = 61.6\text{V}$. Finally, at $t = 1.15\text{s}$, they return to $V_{dc1} = V_{dc2} = V_{dc3} = 66.6\text{V}$.

For closed-loop control, the d_{comp} parameters have been integrated not only into MNRV (D)PWM but also into VVPWM and COPWM. Stable operational characteristics are confirmed across all modulation methods, responding well to step changes in the dc-link voltages. Overall, VVPWM and COPWM demonstrate relatively rapid dynamic responses compared to MNRV (D)PWM. Furthermore, it can be observed that the voltage variations in the values of V_{dc1} and V_{dc3} in VVPWM or COPWM are relatively smaller compared to MNRV (D)PWM. This is probably because VVPWM and COPWM tightly control the voltage deviations at each control cycle, while in MNRV (D)PWM, some degree of voltage deviation is allowed, controlling the voltage deviations every $T/3$ period. An intriguing observation is that

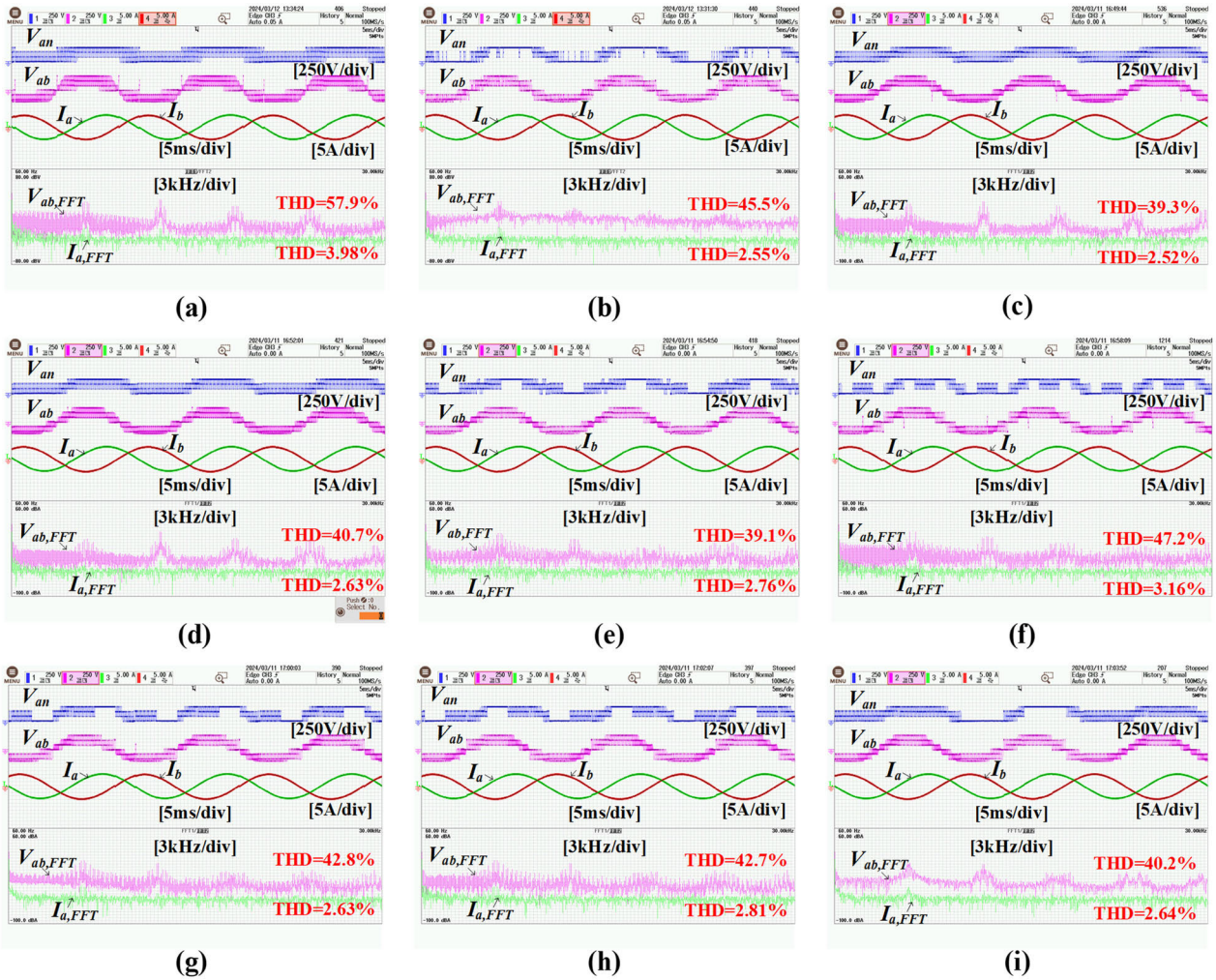


FIGURE 14. Steady state operational waveforms (V_{an} , V_{ab} , I_a , I_b) and harmonics spectrum of V_{ab} and I_a for (a) VVPWM, (b) COPWM, (c) SPWM, (d) SVPWM, (e) 60° DPWM, (f) 30° DPWM, (g) $60^\circ(+30^\circ)$ DPWM, (h) $60^\circ(-30^\circ)$ DPWM, and (i) DPWMMAXorMIN when $m = 0.9$ and $pf = 0.9$.

in the DPWMMAXorMIN method, there are control efforts to overcome forced voltage variations and mitigate voltage imbalances by utilizing clamp mode based on dc-link voltage deviations.

V. EXPERIMENTS

To verify the feasibility of proposed three-phase diode-clamped four-level PWM inverter with offset voltage injection, several experiments were performed under the specified conditions with $V_{dc} = 200V$, $C_{dc} = 7.5mF$, $f_s = 60Hz$, $m_f = 100$, while varying m between 0.3 and 0.9, and varying pf between 0.2 and 0.9.

Fig. 13 illustrates the experimental setup utilized in the prototype test. It encompasses a laptop computer serving as the control unit, the prototype circuit, an oscilloscope, a power analyzer, and an RL load.

Fig. 14 illustrates the main operational waveforms such as V_{an} , V_{ab} , I_a , and I_b under steady-state conditions with a load impedance of 24.3Ω having a $pf = 0.9$ ($R = 21.87 \Omega$,

$L = 28.096mH$ per phase) at $m = 0.9$. Additionally, it includes the FFT results for line voltage (V_{ab}) and phase current (I_a). For comparison, experiments under the same conditions were conducted for conventional VVPWM and COPWM methods. From Figs. 14(a) to (i), each figure exhibits distinctive modulation characteristics derived from the V_{an} waveform. In the case of VVPWM, the THD of V_{ab} is 57.9%, and for I_a , it is 3.98%. The observed higher THD for I_a compared to simulation results is attributed to nonlinear circuit elements and side effects such as dead-time and switching noise, including CM mode noise, which are not dealt with in this paper [39], [40]. In COPWM, intermittent clamping to the maximum (V_{dc}) or minimum (0) occurs in the V_{an} waveform, and it exhibits a more natural stepped waveform shape compared to VVPWM when the polarity of V_{ab} changes. The THD for V_{ab} is 45.5%, and for I_a , it is 2.55%, indicating better performance for both components compared to VVPWM when m is high. Figs. 14(c) to (i) represent the proposed MNRV (D)PWM. The characteristics of MNRV (D)PWM,

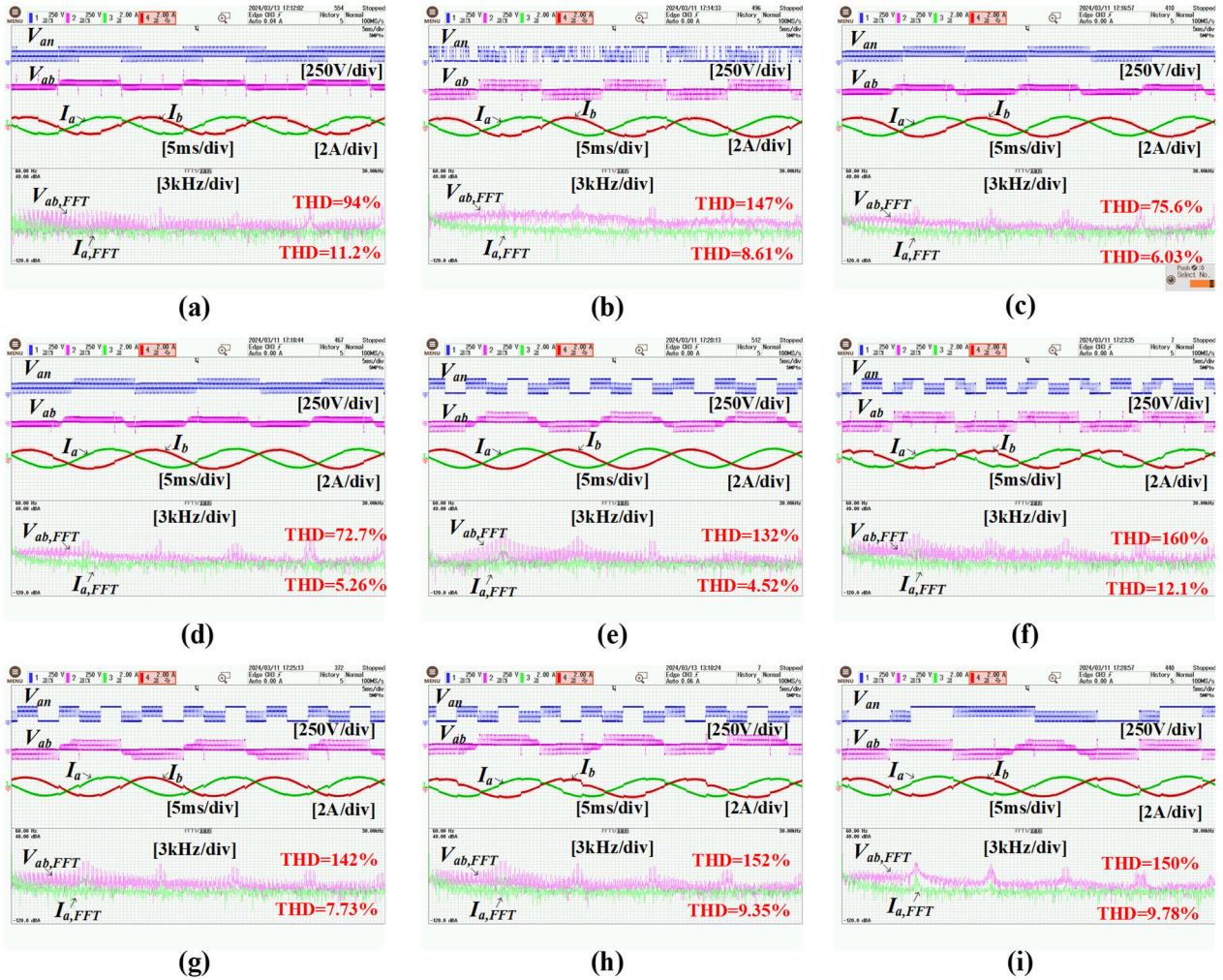


FIGURE 15. Steady state operational waveforms (V_{an} , V_{ab} , I_a , I_b) and harmonics spectrum of V_{ab} and I_a for (a) VVPWM, (b) COPWM, (c) SPWM, (d) SVPWM, (e) 60° DPWM, (f) 30° DPWM, (g) $60^\circ(+30^\circ)$ DPWM, (h) $60^\circ(-30^\circ)$ DPWM, and (i) DPWMMAXorMIN when $m = 0.3$ and $pf = 0.9$.

as outlined in the simulation section, are uniquely observed in the V_{an} waveform. Overall, the THD for V_{ab} ranges from 39.1% to 47.2%, comparable to or lower than COPWM, while the THD for I_a ranges from 2.52% to 3.16%, slightly higher or similar to COPWM.

Fig. 15 depicts the main operational waveforms under steady-state conditions with a $pf = 0.9$ and $m = 0.3$. For VVPWM, the THD of V_{ab} is 94%, and for I_a , it is 11.2%. In contrast, for COPWM, the THD for V_{ab} is 147%, and for I_a , it is 8.61%. It is observed that when m is low, the THD performance of V_{ab} in COPWM deteriorates compared to VVPWM, whereas THD of I_a is superior. Figs. 15(c) to (i) represent the proposed MNRV (D)PWM. Overall, the THD performance of V_{ab} and I_a seems to degrade compared to when m is high. Specifically, the THD for V_{ab} ranges from 72.7% to 160%, while the THD for I_a ranges from 4.52% to 12.1%. This indicates that in 30° DPWM, $60^\circ(-30^\circ)$ DPWM, and DPWMMAXorMIN, higher THD is observed compared to COPWM, whereas in the remaining SPWM, SVPWM,

60° DPWM, and $60^\circ(+30^\circ)$ DPWM, lower THD is observed compared to COPWM. This trend generally aligns with the simulation results.

Figs. 16 and 17 illustrate the experimental results under the conditions of $pf = 0.2$ ($R = 4.86 \Omega$, $L = 63.156\text{mH}$ per phase) for $m = 0.9$ and $m = 0.3$, respectively. Comparing with the results from Figs. 14 and 15, where pf is higher, it appears that overall THD performance of V_{ab} and I_a is better when pf is lower. However, due to the presence of side effects in the circuit, the THD for I_a remains higher compared to simulation values. For $m = 0.9$, in VVPWM, the THD value for V_{ab} was 52.8%, and for I_a , it was 2.26%. In COPWM, the THD values were 44.7% and 2.12% for V_{ab} and I_a respectively. In MNRV (D)PWM, the THD ranged from 37.9% to 44.4% for V_{ab} and from 2.07% to 2.37% for I_a . Meanwhile, for $m = 0.3$, in VVPWM, the THD value for V_{ab} was 81.7%, and for I_a , it was 5.26%. In COPWM, the THD values were 128% and 6.83% for V_{ab} and I_a respectively, showing a significant increase in V_{ab} 's THD compared to

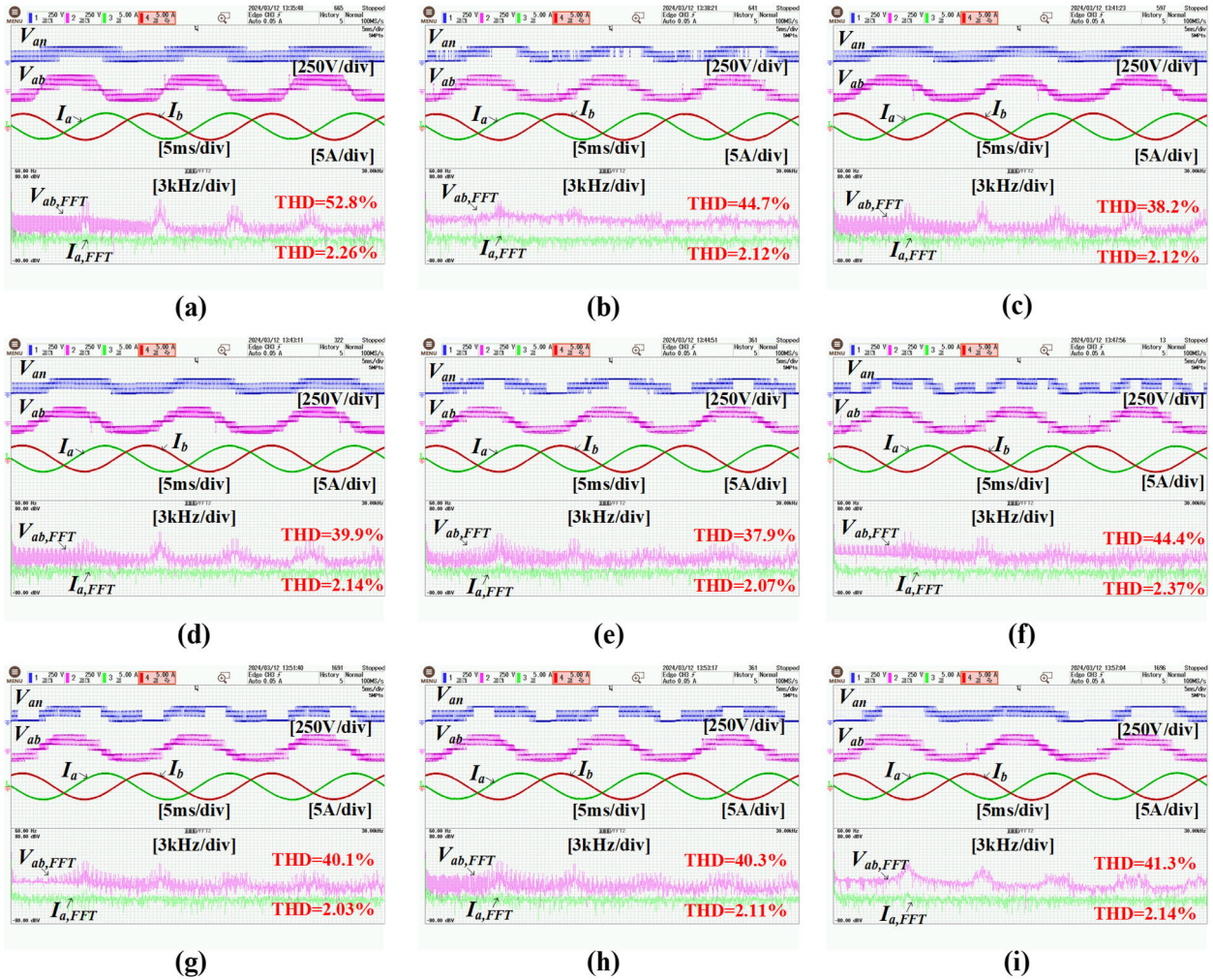


FIGURE 16. Steady state operational waveforms (V_{an} , V_{ab} , I_a , I_b) and harmonics spectrum of V_{ab} and I_a for (a) VVPWM, (b) COPWM, (c) SPWM, (d) SVPWM, (e) 60° DPWM, (f) 30° DPWM, (g) $60^\circ(+30^\circ)$ DPWM, (h) $60^\circ(-30^\circ)$ DPWM, and (i) DPWMMAXorMIN when $m = 0.9$ and $pf = 0.2$.

VVPWM. In MNRV (D)PWM, the THD for V_{ab} ranged from 64.6% to 139%, while the THD for I_a ranged from 3.03% to 5.27%, showing superior performance compared to VVPWM and COPWM.

Overall, waveform quality analysis of line voltage and phase current for $pf = 0.2/0.9$ and $m = 0.3/0.9$ shows that MNRV (D)PWM outperforms existing methods in terms of power quality.

Figs. 18 and 19 depict the transient characteristics observed when m suddenly transitions from 0.3 to 0.9 under conditions of $pf = 0.9$ and $pf = 0.2$ respectively. Due to the limitation of the oscilloscope's simultaneous measurement channels, V_{dc1} , V_{dc2} , V_{dc3} , and I_a were initially measured during the m transition condition. Subsequently, I_a , V_{an} , and V_{offset} were measured again under the same conditions, and the waveforms were overlaid to compare. The MNRV (D)PWM methods used in the experiments can be distinguished from the V_{an} and V_{offset} waveforms. It is evident that the dc-link voltages are well balanced and regulated when m undergoes

sudden changes under all experimental conditions. Moreover, the current exhibits stable operation with minimal distortion during transient periods.

Figs. 20 and 21 demonstrate the dynamic behavior observed when the dc-link reference voltages fluctuate under the conditions of $m = 0.9$, $pf = 0.9$, and $m = 0.9$, $pf = 0.2$, respectively. Similar to Fig. 12, all dc-link voltage references were initially fixed at 66.6V. However, subsequently, they were adjusted to $V_{dc1} = 71.6V$, $V_{dc2} = 61.6V$, and $V_{dc3} = 66.6V$. After a stabilization period, all reference voltages reverted to 66.6V. Subsequently, following another stabilization period, the reference voltages were adjusted to $V_{dc1} = 71.6V$, $V_{dc2} = 66.6V$, and $V_{dc3} = 61.6V$, before being readjusted back to 66.6V. To distinguish between the applied modulation methods, the DAC output values for $d_{E,a}$ were included.

Despite slight differences in stabilization time compared to simulations, the system demonstrates stable transient characteristics and maintains a balanced dc-link voltage after

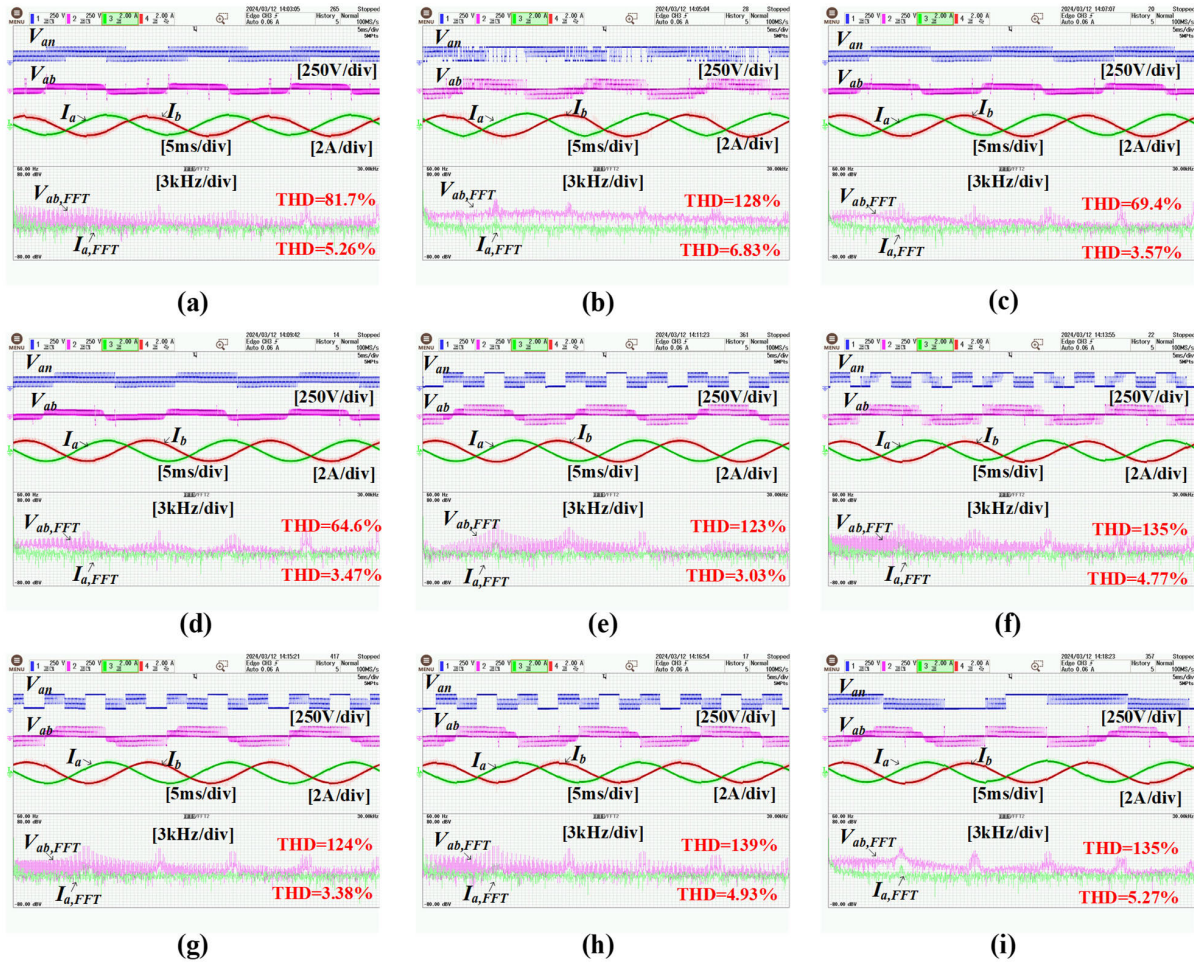


FIGURE 17. Steady state operational waveforms (V_{an} , V_{ab} , I_a , I_b) and harmonics spectrum of V_{ab} and I_a for (a) VVPWM, (b) COPWM, (c) SPWM, (d) SVPWM, (e) 60°DPWM, (f) 30°DPWM, (g) 60°(+30°)DPWM, (h) 60°(-30°)DPWM, and (i) DPWMMAXorMIN when $m = 0.3$ and $pf = 0.2$.

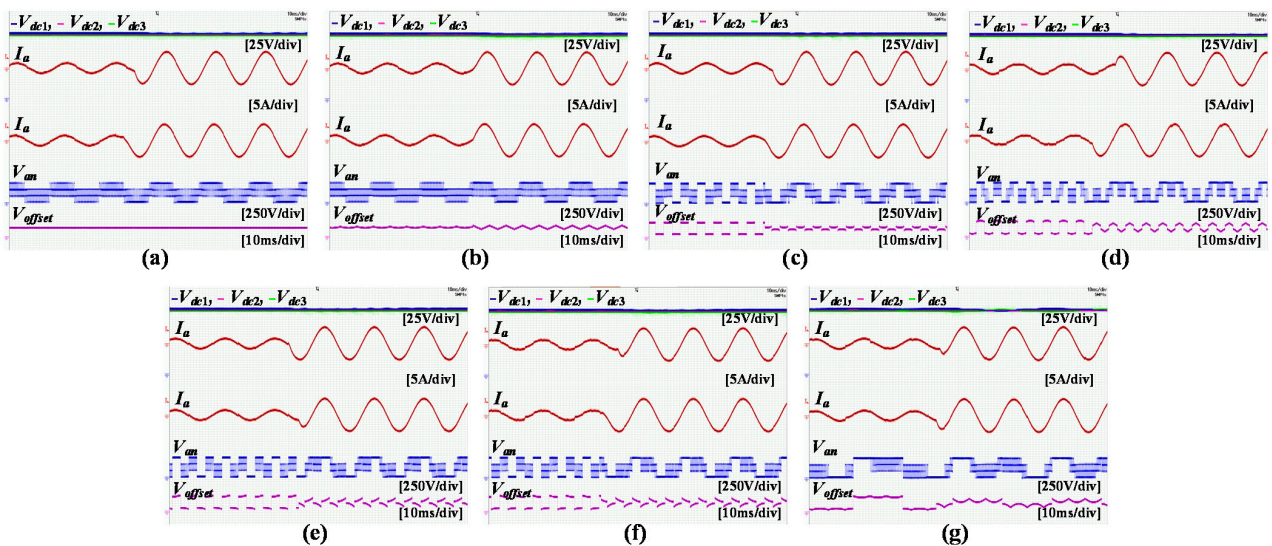


FIGURE 18. Dynamic performance of (a) SPWM, (b) SVPWM, (c) 60°DPWM, (d) 30°DPWM, (e) 60°(+30°)DPWM, (f) 60°(-30°)DPWM, and (g) DPWMMAXorMIN when m suddenly changes from 0.3 to 0.9 with $pf = 0.9$.

fluctuations under all conditions, indicating well-controlled behavior.

Based on the characteristics observed under both normal and transient conditions, it has been confirmed that

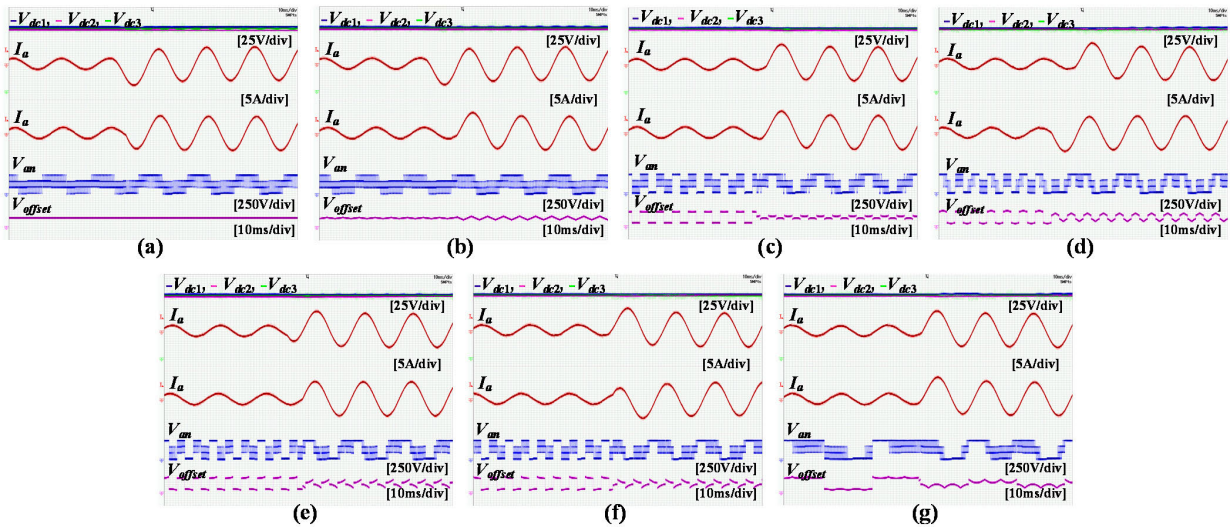


FIGURE 19. Dynamic performance of (a) SPWM, (b) SVPWM, (c) 60° DPWM, (d) 30° DPWM, (e) 60°(+30°) DPWM, (f) 60°(-30°) DPWM, and (g) DPWMMAXorMIN when m suddenly changes from 0.3 to 0.9 with $pf = 0.2$.

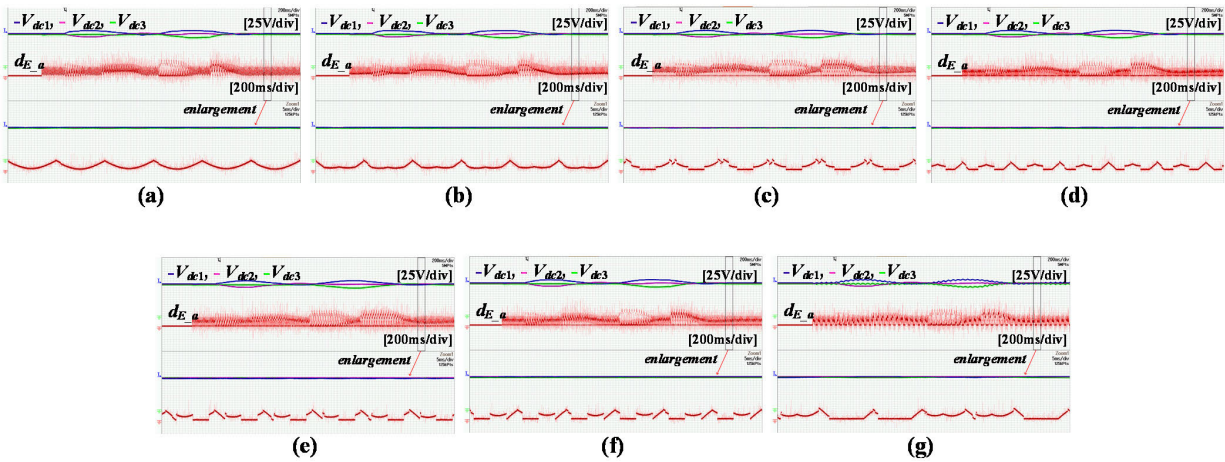


FIGURE 20. Dynamics of dc-link voltage step changes for (a) SPWM, (b) SVPWM, (c) 60° DPWM, (d) 30° DPWM, (e) 60°(+30°) DPWM, (f) 60°(-30°) DPWM, and (g) DPWMMAXorMIN when $m = 0.9$ and $pf = 0.9$.

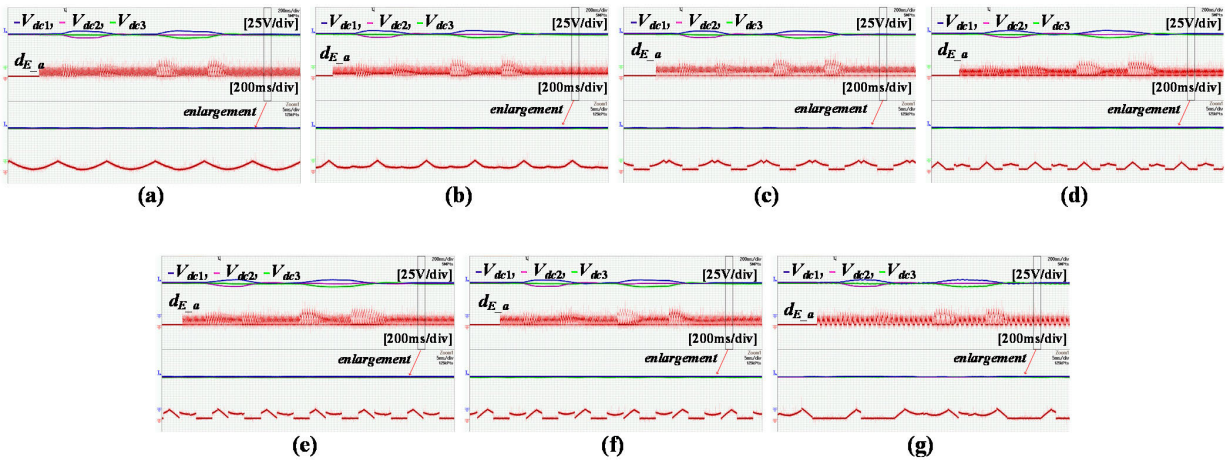


FIGURE 21. Dynamics of dc-link voltage step changes for (a) SPWM, (b) SVPWM, (c) 60° DPWM, (d) 30° DPWM, (e) 60°(+30°) DPWM, (f) 60°(-30°) DPWM, and (g) DPWMMAXorMIN when $m = 0.9$ and $pf = 0.2$.

the proposed offset voltage injection-based MNRV (D)PWM operates effectively. The analysis of THD in line voltage

and phase current indicates superior performance compared to conventional methods such as VVPWM and COPWM.

Additionally, it has been observed that the system exhibits stable operational characteristics even when m varies or dc-link reference voltages fluctuate.

VI. CONCLUSION

In this paper, a three-phase diode-clamped four-level PWM inverter based on offset voltage injection utilizing the MNRV (D)PWM methods was proposed. MNRV(D)PWM evenly utilizes multiple adjacent vectors to adjust the charge/discharge characteristics of the dc-link capacitors and fine-tune the duty ratios of the reference vectors to satisfy the *volt-time* product. Additionally, duty compensators proportional to the dc-link voltage deviations are designed to balance the dc-link voltage while facilitating easy closed-loop control. Furthermore, various (D)PWM methods based on the offset voltage injection methods were presented.

By extending the methodology applied to the four-level inverter, a general MNRV (D)PWM method applicable to general high-dimensional multilevel multiphase PWM inverters was also proposed. Additionally, while discussing the characteristics and differences between dc/dc converters and dc/ac inverters using the MNRV (D)PWM method, the generality of MNRV (D)PWM applicable not only to dc/ac but also to dc/dc was demonstrated. Through ΔV_{dc} analysis, it was confirmed that the ripple component of the dc-link voltage generated by the offset voltage injection method is related to the three-phase summation of the product of the duty of the E voltage level vector and the phase current.

Various simulations and experiments have confirmed the efficacy of the proposed method compared to well-established multilevel inverter schemes such as VVPWM and COPWM. While exhibiting a lower average switching frequency, the proposed method demonstrates superior performance in terms of THD for line-to-line voltages and phase currents, particularly at higher m values. Effective control over fluctuations in the dc-link voltage reference and maintenance of voltage balancing were also verified.

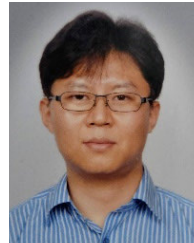
REFERENCES

- [1] J. Rodriguez, J.-S. Lai, and F. Z. Peng, "Multilevel inverters: A survey of topologies, controls, and applications," *IEEE Trans. Ind. Electron.*, vol. 49, no. 4, pp. 724–738, Aug. 2002.
- [2] S. Kouro, M. Malinowski, K. Gopakumar, J. Pou, L. G. Franquelo, B. Wu, J. Rodriguez, M. A. Pérez, and J. I. Leon, "Recent advances and industrial applications of multilevel converters," *IEEE Trans. Ind. Electron.*, vol. 57, no. 8, pp. 2553–2580, Aug. 2010.
- [3] K. K. Gupta, A. Ranjan, P. Bhatnagar, L. K. Sahu, and S. Jain, "Multilevel inverter topologies with reduced device count: A review," *IEEE Trans. Power Electron.*, vol. 31, no. 1, pp. 135–151, Jan. 2016.
- [4] M. A. Perez, S. Ceballos, G. Konstantinou, J. Pou, and R. P. Aguilera, "Modular multilevel converters: Recent achievements and challenges," *IEEE Open J. Ind. Electron. Soc.*, vol. 2, pp. 224–239, 2021.
- [5] A. Nami, F. Zare, A. Ghosh, and F. Blaabjerg, "A hybrid cascade converter topology with series-connected symmetrical and asymmetrical diode-clamped H-bridge cells," *IEEE Trans. Power Electron.*, vol. 26, no. 1, pp. 51–65, Jan. 2011.
- [6] T. Modeer, N. Pallo, T. Foulkes, C. B. Barth, and R. C. N. Pilawa-Podgurski, "Design of a GaN-based interleaved nine-level flying capacitor multilevel inverter for electric aircraft applications," *IEEE Trans. Power Electron.*, vol. 35, no. 11, pp. 12153–12165, Nov. 2020.
- [7] A. K. Koshti and M. N. Rao, "A brief review on multilevel inverter topologies," in *Proc. Int. Conf. Data Manage., Anal. Innov. (ICDMAI)*, Feb. 2017, pp. 187–193.
- [8] J. Pou, R. Pindado, and D. Boroyevich, "Voltage-balance limits in four-level diode-clamped converters with passive front ends," *IEEE Trans. Ind. Electron.*, vol. 52, no. 1, pp. 190–196, Feb. 2005.
- [9] C. Gao, X. Jiang, Y. Li, Z. Chen, and J. Liu, "A DC-link voltage self-balance method for a diode-clamped modular multilevel converter with minimum number of voltage sensors," *IEEE Trans. Power Electron.*, vol. 28, no. 5, pp. 2125–2139, May 2013.
- [10] J. Ebrahimi, H. Karshenas, and A. Bakhshai, "A five-level nested diode-clamped converter for medium-voltage applications," *IEEE Trans. Ind. Electron.*, vol. 69, no. 7, pp. 6471–6483, Jul. 2022.
- [11] A. Ajami, H. Shokri, and A. Mokhberdoran, "Parallel switch-based chopper circuit for DC capacitor voltage balancing in diode-clamped multilevel inverter," *IET Power Electron.*, vol. 7, no. 3, pp. 503–514, Mar. 2014.
- [12] X. Liu, J. Lv, C. Gao, Z. Chen, Y. Guo, Z. Gao, and B. Tai, "A novel diode-clamped modular multilevel converter with simplified capacitor voltage-balancing control," *IEEE Trans. Ind. Electron.*, vol. 64, no. 11, pp. 8843–8854, Nov. 2017.
- [13] Z. Shu, X. He, Z. Wang, D. Qiu, and Y. Jing, "Voltage balancing approaches for diode-clamped multilevel converters using auxiliary capacitor-based circuits," *IEEE Trans. Power Electron.*, vol. 28, no. 5, pp. 2111–2124, May 2013.
- [14] K. Sano and H. Fujita, "Voltage-balancing circuit based on a resonant switched-capacitor converter for multilevel inverters," *IEEE Trans. Ind. Appl.*, vol. 44, no. 6, pp. 1768–1776, Nov./Dec. 2008.
- [15] A. Shukla, A. Ghosh, and A. Joshi, "Flying-capacitor-based chopper circuit for DC capacitor voltage balancing in diode-clamped multilevel inverter," *IEEE Trans. Ind. Electron.*, vol. 57, no. 7, pp. 2249–2261, Jul. 2010.
- [16] I. Harbi, J. Rodriguez, E. Liegmann, H. Makhmreh, M. L. Heldwein, M. Novak, M. Rossi, M. Abdelrahem, M. Trabelsi, M. Ahmed, P. Karamanakos, S. Xu, T. Dragicevic, and R. Kennel, "Model predictive control of multilevel inverters: Challenges, recent advances, and trends," *IEEE Trans. Power Electron.*, vol. 38, no. 9, pp. 10845–10868, Sep. 2023.
- [17] V. Yaramasu, B. Wu, M. Rivera, M. Narimani, S. Kouro, and J. Rodriguez, "Generalised approach for predictive control with common-mode voltage mitigation in multilevel diode-clamped converters," *IET Power Electron.*, vol. 8, no. 8, pp. 1440–1450, Aug. 2015.
- [18] V. Yaramasu and B. Wu, "Model predictive decoupled active and reactive power control for high-power grid-connected four-level diode-clamped inverters," *IEEE Trans. Ind. Electron.*, vol. 61, no. 7, pp. 3407–3416, Jul. 2014.
- [19] M. A. Saqib and S. A. R. Kashif, "Artificial neural network based space vector PWM for a five-level diode-clamped inverter," in *Proc. 20th Australas. Universities Power Eng. Conf.*, Dec. 2010, pp. 1–6.
- [20] S. Zhao, F. Blaabjerg, and H. Wang, "An overview of artificial intelligence applications for power electronics," *IEEE Trans. Power Electron.*, vol. 36, no. 4, pp. 4633–4658, Apr. 2021.
- [21] M. Mehra, M. Babaie, M. Sharifzadeh, and K. Al Haddad, "An input-output feedback linearization control method synthesized by artificial neural network for grid-tied packed E-cell inverter," *IEEE Trans. Ind. Appl.*, vol. 57, no. 3, pp. 3131–3142, May/June 2021.
- [22] S. Busquets-Monge, J. Bordonau, D. Boroyevich, and S. Somavilla, "The nearest three virtual space vector PWM—A modulation for the comprehensive neutral-point balancing in the three-level NPC inverter," *IEEE Power Electron. Lett.*, vol. 2, no. 1, pp. 11–15, Mar. 2004.
- [23] S. Busquets-Monge, S. Alepuz, J. Bordonau, and J. Peracaula, "Voltage balancing control of diode-clamped multilevel converters with passive front-ends," *IEEE Trans. Power Electron.*, vol. 23, no. 4, pp. 1751–1758, Jul. 2008.
- [24] S. Busquets-Monge, S. Alepuz, J. Rocabert, and J. Bordonau, "Pulsewidth modulations for the comprehensive capacitor voltage balance of n -level three-leg diode-clamped converters," *IEEE Trans. Power Electron.*, vol. 24, no. 5, pp. 1364–1375, May 2009.
- [25] S. Xia, X. Wu, J. Zheng, X. Li, and K. Wang, "A virtual space vector PWM with active neutral point voltage control and common mode voltage suppression for three-level NPC converters," *IEEE Trans. Ind. Electron.*, vol. 68, no. 12, pp. 11761–11771, Dec. 2021.

- [26] S. Busquets-Monge, R. Maheshwari, J. Nicolas-Apruzzese, E. Lupon, S. Munk-Nielsen, and J. Bordonau, "Enhanced DC-link capacitor voltage balancing control of DC-AC multilevel multileg converters," *IEEE Trans. Ind. Electron.*, vol. 62, no. 5, pp. 2663–2672, May 2015.
- [27] K. Wang, Z. Zheng, and Y. Li, "A novel carrier-overlapped PWM method for four-level neutral-point clamped converters," *IEEE Trans. Power Electron.*, vol. 34, no. 1, pp. 7–12, Jan. 2019.
- [28] K. Wang, Z. Zheng, L. Xu, and Y. Li, "A generalized carrier-overlapped PWM method for neutral-point-clamped multilevel converters," *IEEE Trans. Power Electron.*, vol. 35, no. 9, pp. 9095–9106, Sep. 2020.
- [29] K. Wang, Z. Zheng, and Y. Li, "Topology and control of a four-level ANPC inverter," *IEEE Trans. Power Electron.*, vol. 35, no. 3, pp. 2342–2352, Mar. 2020.
- [30] M. Wu, Y. W. Li, H. Tian, Y. Li, and K. Wang, "Modified carrier-overlapped PWM with balanced capacitors and eliminated dead-time spikes for four-level NNPC converters under low frequency," *IEEE J. Emerg. Sel. Topics Power Electron.*, vol. 10, no. 6, pp. 6832–6844, Dec. 2022.
- [31] M.-S. Song, "Multi-neighboring reference vector discontinuous PWM based on compensation for voltage deviation of DC-link capacitors applicable for single-phase NPC multi-level PWM converter," *J. Korean Soc. Railway*, vol. 21, no. 4, pp. 349–362, May 2018.
- [32] M.-S. Song and J.-B. Lee, "Pulse-amplitude-modulation full-bridge diode-clamped multilevel LLC resonant converter using multi-neighboring reference vector discontinuous PWM," *Energies*, vol. 15, no. 11, p. 4045, May 2022.
- [33] M.-S. Song, J. Kim, and J.-B. Lee, "Full-bridge diode-clamped four-level symmetric switching converter," *IEEE Access*, vol. 11, pp. 103350–103363, 2023.
- [34] M.-S. Song, "Pulse-amplitude-modulation full-bridge diode-clamped three-level LLC resonant converter with offset voltage injection method," *Trans. Korean Inst. Electr. Eng.*, vol. 71, no. 9, pp. 1342–1350, 2022.
- [35] M.-S. Song, J.-B. Lee, H. Jung, and H. Kim, "Half-bridge diode-clamped four-level LLC resonant converter with pulse-amplitude-modulation for railway applications," *J. Elect. Eng. Technol.*, vol. 18, pp. 4481–4497, May 2023.
- [36] E.-S. Jun, M. H. Nguyen, and S.-S. Kwak, "Model predictive control method with NP voltage balance by offset voltage injection for three-phase three-level NPC inverter," *IEEE Access*, vol. 8, pp. 172175–172195, 2020.
- [37] J. Pou, J. Zaragoza, S. Ceballos, M. Saeedifard, and D. Boroyevich, "A carrier-based PWM strategy with zero-sequence voltage injection for a three-level neutral-point-clamped converter," *IEEE Trans. Power Electron.*, vol. 27, no. 2, pp. 642–651, Feb. 2012.
- [38] A. M. Hava, R. Kerkman, and T. A. Lipo, "A high-performance generalized discontinuous PWM algorithm," *IEEE Trans. Ind. Appl.*, vol. 34, no. 5, pp. 1059–1071, Sep./Oct. 1998.
- [39] S.-H. Hwang and J.-M. Kim, "Dead time compensation method for voltage-fed PWM inverter," *IEEE Trans. Energy Convers.*, vol. 25, no. 1, pp. 1–10, Mar. 2010.
- [40] D. Jiang, F. Wang, and J. Xue, "PWM impact on CM noise and AC CM choke for variable-speed motor drives," *IEEE Trans. Ind. Appl.*, vol. 49, no. 2, pp. 963–972, Mar. 2013.



MIN-SUP SONG received the B.S., M.S., and Ph.D. degrees from the Department of Electrical Engineering, Pohang University of Science and Technology, Pohang, South Korea, in 2005, 2007, and 2011, respectively. He was a Senior Researcher with LG Display, Samsung Electro-Mechanics, and Hyundai-Rotem, South Korea, from 2011 to 2016. He is currently a Senior Researcher with the Smart Electrical and Signaling Division, Korea Railroad Research Institute, Uiwang-si, South Korea. His research interests include the development of novel circuit topologies and suitable switching modulation techniques for high-power and high-voltage power conversion systems.



JAEWON KIM received the B.S., M.S., and Ph.D. degrees in electrical engineering from Korea University, Seoul, South Korea, in 2006, 2008, and 2018, respectively. He is currently a Principal Researcher with Korea Railroad Research Institute, Uiwang-si, South Korea. His research interests include onboard energy storage systems for railway trains, traction power supply system analysis, and railway electric components reliability analysis.



HWAN-HEE CHO received the B.S. degree from the School of Electrical Engineering, Dankook University, Yongin-si, South Korea, in 2014, and the M.S. and Ph.D. degrees in electrical engineering from Korea University, Seoul, South Korea, in 2020. He is currently a Senior Researcher with the Smart Electrical and Signaling Division, Korea Railroad Research Institute, Uiwang-si, South Korea.

• • •